Search for Supersymmetry with the Dilepton Final State at the ATLAS Experiment

Muhammad Aftab Alam

Department of Physics

Royal Holloway, University of London

A thesis submitted to the University of London for the

Degree of Doctor of Philosophy

January 20, 2012

Declaration

I confirm that the work presented in this thesis is my own. Where information has been derived from other sources, I confirm that this has been indicated in the document.

Muhammad Aftab Alam

Abstract

The main theme of this thesis is the design of a search for Supersymmetry in the ATLAS Experiment using events with two opposite sign leptons, two jets and missing transverse energy in the final state. This study has been performed within the framework of the mSUGRA model. The most significant background in this channel is from events with a top-antitop ($t\bar{t}$) quark pair, where the $t\bar{t}$ decays result in two W bosons that each decay into a lepton and a neutrino. The bulk of the analysis is devoted to developing a data-driven method to estimate the top background using a control sample. The $t\bar{t}$ control sample has been constructed by selecting events with one lepton and four jets. Two of these jets may come from a W boson decay, and these are identified using kinematic and flavour tag information. By replacing the W boson's jets with a simulated lepton-neutrino pair, one obtains a $t\bar{t}$ event with characteristics that should be very close to the $t\bar{t}$ background of the dilepton search. The distributions of kinematic variables for background events in the search region are also compared with those of the control sample, and they are found in reasonably good agreement when the jets are correctly identified. The analysis has been tested using simulated data. A statistical analysis based on the profile-likelihood method has been developed for the search. For a data sample of a given size, the expected discovery significance and upper limits on signal cross sections are investigated.

Acknowledgements

At first, I wish to express my profound gratitude to my supervisor, Dr. Glen Cowan, for his guidance, support and encouragement throughout my PhD.

I would like to thank the Science and Technology Facilities Council (STFC) for providing financial support during this degree. I am also grateful to Royal Holloway for providing funding for several essential conference trips.

I am also very thankful to the Particle Physics Group at Royal Holloway for the help they provided. I would like to thank Dr. Simon George for setting up software packages and for answering many questions regarding this.

To my wife Mahwash and son Ajlaal.

Contents

List of Figures

List of Tables

Chapter 1

Introduction

Despite its great success, there are a number of reasons to believe that the Standard Model (SM) of particle physics is incomplete. Supersymmetry is one alternative to extend the Standard Model, which looks quite appealing specifically the way it tackles the hierarchy problem. It proposes new massive particles but none of them has been observed. One of the main goals of the ATLAS experiment at the Large Hadron Collider is to explore new physics (such as Supersymmetry) at the TeV scale.

The main theme of this thesis is the design of a search for Supersymmetry in the ATLAS experiment by requiring events with two opposite-sign leptons, two jets and missing transverse energy in the final state. This analysis has been performed within the framework of the mSUGRA model, and it is based on 7 TeV centre-of-mass energy using Monte Carlo data based on a full simulation of the detector. For this study, a benchmark point, SU4, is chosen in the mSUGRA parameter space. The analysis described here takes ATLAS's official dilepton analysis [1] as a starting point, and it is reviewed with slight modification. The Monte Carlo samples used in the thesis are centrally produced within the ATLAS collaboration.

The most significant background in this channel is from events with a top-antitop ($t\bar{t}$) quark pair, where the $t\bar{t}$ decays result in two W bosons that each decay into a lepton and

a neutrino. In order to claim a SUSY discovery, the Standard Model backgrounds are estimated by data driven methods. In this thesis, the bulk of the analysis is devoted to develop a data driven method for estimating the $t\bar{t}$ background in the signal region. To do this, a control sample of $t\bar{t}$ events has been constructed by selecting events with one lepton and four jets, i.e., one of the above W bosons decays hadronically to populate the final state with two additional jets. Later, these additional jets (here called W jets) are replaced with a simulated lepton and a neutrino. The correct identification of 2 W jets is a challenging task, which uses both kinematic and flavour tag information. The Monte Carlo studies indicate that the identified W jets are correct in 51 % of the events selected in the control sample. The fraction is not very high because the 2 W jets survived the selection cuts only 59 % of the cases. When the 2 W jets are accepted in the control sample, the method identifies them 87 % of the time. The distributions from $t\bar{t}$ in the dilepton search channel to those from $t\bar{t}$ in the control sample are compared, and it has been found that the distribution shapes are strongly dependent on the correct identification of the 2 W jets.

The analysis has been tested using simulated data corresponding to an integrated luminosity of $0.5\,\mathrm{fb}^{-1}$. A statistical analysis based on the profile-likelihood method has been developed for the search. For a data sample of $0.5\,\mathrm{fb}^{-1}$, the median discovery significance for the benchmark point SU4 in the mSUGRA parameter space was found to be 2.1. Assuming the absence of a SUSY signal, the median upper limit on the cross section for SUSY (SU4) is 0.59 times the predicted cross section, which is to say one would expect to exclude this model.

The theoretical foundation behind the analysis is presented in Chapter 2. Chapter 3 provides a brief overview of the ATLAS detector. Reconstruction of physics objects in ATLAS is the aim of Chapter 4. In Chapter 5, the analysis overview of the SUSY search based on the dilepton channel is provided. Chapter 6 presents a novel data driven technique which has been developed for estimating the $t\bar{t}$ background. This techinque

has been tested using the mock data in Chapter 7. Finally, the conclusions are drawn in Chapter 8.

Chapter 2

Theory and Motivation

This chapter provides an overview of the theoretical foundation behind the analysis presented in this thesis. At first, we will focus on the Standard Model of particle physics which identifies the building blocks of matter and describes the interactions that bind them. The model is quite successful in explaining essentially all experimental observations made to date. Nevertheless, it is widely believed that this can not be the ultimate theory of nature as it leaves many questions unanswered. One possible extension to the Standard Model is Supersymmetry which may provide answers to some questions that are raised against the Standard Model. The latter part of this chapter is devoted to the discussion on Supersymmetry.

2.1 Standard Model of Particle Physics

The most important conceptual advances in physics in the last century were the special theory of relativity and quantum mechanics, both of which were fused to create relativistic quantum field theory. The Standard Model (SM) [2], [3], [4] which encapsulates our current view of particle physics, has been developed using the framework of quantum field theory. The SM was developed in the 1960s and early 1970s and it has been highly

successful in describing almost all the data that has come from various experiments in the last few decades. In the SM, elementary particles are divided into fermions (half-integral spin) and bosons (integral spin). The fermions are the matter particles while bosons are force carriers that communicate the forces between the fermions. Out of four known forces of nature, three are successfully incorporated in the SM: electromagnetic, strong and weak. The Standard Model is a renormalizable theory, which means calculations in perturbation theory give finite results.

2.1.1 Matter Particles

The fermions in the Standard Model are divided into quarks and leptons. The strongly interacting fermions are called quarks. The quarks also interact via electromagnetic and weak forces. There are six types of quarks called up (u), down (d), charm (c), strange (s), bottom (b) and top (t), and they are arranged into three generations as shown in Table 2.1. In the SM, the fermions of ordinary matter are electron, up-quark and down-quark. The quarks are not free particles. Instead they appear as bound state of quarks called hadrons; for example, the proton and neutron are made up off three quarks, (uud) and (udd) respectively. The quarks carry fractional electric charge i.e. $\frac{2}{3}$ and $-\frac{1}{3}$ in units of the electron's charge. In addition to this, they also possess strong charge called colour. A quark can carry either red, blue or green colour. A particle must carry colour charge in order to interact strongly. Quarks also carry a quantum number called baryon number, which is $+\frac{1}{3}$ for quarks and $-\frac{1}{3}$ for antiquarks.

The leptons also interact through electromagnetic and weak forces but they are immune to the strong interaction because they do not carry colour charge. Like quarks, the leptons are of six types called electron (e), electron-neutrino (ν_e), muon (μ), muon-neutrino (ν_μ), tau (τ) and tau-neutrino (ν_τ) which are organised into three generations as shown in Table 2.2. Muons and taus are the heavier versions of electrons, i.e., they have identical properties to electrons except for their mass. All charged leptons have

Generations	Quarks	Charge (/e)	Mass
1^{st}	up (u)	$+\frac{2}{3}$	1.53 - 3.3 MeV
	down (d)	$-\frac{1}{3}$	3.5 - 6.0 MeV
2^{nd}	charm (c)	$+\frac{2}{3}$	1.27 GeV
	strange (s)	$-\frac{1}{3}$	104 MeV
3^{rd}	top (t)	$+\frac{2}{3}$	171.2 GeV
	bottom (b)	$-\frac{1}{3}$	4.2 GeV

Table 2.1: Quarks and their properties. Numbers taken from [5].

Generations	Leptons	Charge (/e)	Mass
1^{st}	electron (e)	-1	0.511 MeV
	electron-neutrino (ν_e)	0	~ 0
2^{nd}	muon (μ)	-1	105.7 MeV
	muon-neutrino (ν_μ)	0	~ 0
3^{rd}	tau (τ)	-1	1.78 GeV
	tau-neutrino (ν_τ)	0	~ 0

Table 2.2: Leptons and their properties. Numbers taken from [5].

their own neutrinos, which are massless in the context of the original Standard Model. Recently, the phenomena of neutrino oscillations has given the evidence of non-zero neutrino mass [6], [7], [8]. Unlike charged leptons, the neutrinos interact only weakly as they are electrically neutral. Leptons also carry a quantum number called lepton number, which is +1 for particles and -1 for antiparticles.

2.1.2 Force Carriers

In the SM, the forces are described as exchange of spin-1 vector bosons (also called force-carriers) between the fermions. All SM interactions have their own vector bosons and their properties are shown in Table 2.3. The electromagnetic interaction is mediated by photon (γ) and the part of the SM that explores the dynamics of particles in this

Coupling	Vector Bosons	Charge (/e)	Mass
electromagnetic	photon (γ)	0	0
strong	gluons (g)	0	0
weak	$W^{\pm}, Z$	$\pm 1, 0$	80.4 GeV, 91.2 GeV

Table 2.3: Force-carriers and their properties. Numbers taken from [5].

interaction is called quantum electrodynamics (QED). In QED, the photon couples to all the charged particles of the SM. The part of the SM responsible for strong interaction is known as quantum chromodynamics (QCD). The force carrier of strong interaction is gluon (g) which is electrically neutral and massless. Like quarks, the gluon also possess colour.

The mediators of the weak interaction are W^+, W^- and Z bosons. Unlike photon and gluon, they are massive of the order of 100 GeV as shown in Table 2.3. It is predicted that W and Z bosons obtain their masses by the phenomenon of Higgs mechanism that will be discussed in the next section. Moreover, the electromagnetic and weak forces are unified and described as one electroweak (EW) force at high energies. This EW symmetry breaks down when weak bosons acquire masses as a result of Higgs mechanism. At energies of about 10^{16} GeV, all the SM forces are expected to be unified, and described as Grand Unified Theory (GUT). Finally, the gravitons are also postulated as the force carriers of the gravitational interaction but the SM does not include gravity.

2.1.3 The Higgs Mechanism

It is mentioned in the previous section that the SM forces are described as exchange of spin-1 particles. A fundamental symmetry, called gauge invariance, is associated with theories in which force-carriers are spin-1 particles. The gauge invariance requires these force-carriers to be massless if they are the only bosons in the theory. This criterion is satisfied by the electromagnetic and strong forces where photons and gluons are massless. But the problem is W and Z bosons are massive, and the weak force cannot be gauge

invariant if they are the only bosons present. This problem is rectified by the Higgs mechanism. The Higgs mechanism introduces a hypothetical field called the Higgs field and it predicts that the particles (bosons and fermions) acquire masses by interacting with this field. The Higgs field is a quantum field but it is unlike any other field, for example, it has non-zero vacuum expectation value[1] while the electromagnetic field has zero value. Moreover, Higgs mechanism predicts a spin-0 particle called the Higgs boson. The Higgs boson is a quantum of the Higgs field, like photon is a quantum of electromagnetic field. The Higgs boson is the only undiscovered particle which is required by the SM. Direct searches of Higgs at the Large Electron-Positron Collider (LEP), which was one of the largest particle accelerator and was used from 1989 until 2000, have established that the Higgs boson must have a mass greater than 114.4 GeV [10]. Recent searches of Higgs at the Tevatron, which is the second highest energy accelerator in the world after the Large Hadron Collider, exclude the Higgs boson mass in the range 156 - 177 GeV [11].

2.1.4 Limitations

The SM is a highly successful theory as its predictions are very well tested and experimentally verified. But despite its great success, it has serious limitations that demand one to explore new avenues for its extension. There are a number of problems found in the SM, such as: the SM does not provide a solution to the hierarchy problem (this will be explained below); unification of forces is not possible in its framework; no SM particle is eligible to be considered as a possible candidate for cold dark matter.

Supersymmetry is a possible extension to the SM that attempts to answer some of these questions. In the next section, we will discuss what supersymmetry is and how it tackles the above problems.

[1] In most other cases in physics the vacuum is a state with zero average field [9].

2.2 Supersymmetry

Today, there are several candidate scenarios for physics Beyond the Standard Model (BSM) but Supersymmetry (SUSY) is perhaps the best motivated. SUSY introduces a new symmetry between fermions and bosons which is consistent with the gauge symmetries on which the SM is based. SUSY allows unification of gauge boson couplings at the Grand Unification scale. It is an essential element of string theories and also provides a candidate particle for the universe cold dark matter [12], [13]. In spite of these motivations, no supersymmetric particle has ever been observed.

2.2.1 Motivation

The Hierarchy Problem

We have seen that the Higgs mechanism predicts a spin-0 particle called the Higgs boson. In quantum field theory, the Higgs boson mass is subject to quantum corrections. These corrections can become much larger than the Higgs mass itself. This is the *hierarchy problem*. In the SM, a typical one-loop correction to the Higgs mass is [14]

$$\delta m_H^2 \ \sim \ \mathcal{O}(\frac{\alpha}{\pi})\Lambda^2, \tag{2.1}$$

where m_H is the Higgs mass, α is the coupling strength and Λ is the energy cutoff scale of new physics. It is clear from the above equation that the quantum corrections would be much larger than the Higgs mass if Λ is set to the Planck mass scale, i.e., if Λ is about 10^{19} GeV. This problem can be rectified in SUSY by postulating equal number of fermion F and boson B loops with equal coupling strength. The fermion and boson loops have opposite sign and Equation 2.1 is replaced by

$$\delta m_H^2 \ \sim \ \mathcal{O}(\frac{\alpha}{\pi})\ (m_B^2 - m_F^2), \tag{2.2}$$

The corrections to the Higgs mass is comparable if

$$|m_B^2 - m_F^2| \sim 1\,\mathrm{TeV}^2. \tag{2.3}$$

Unification of Forces

In a quantum theory, one can calculate how a force would behave if one could study it at smaller distances (or higher energies). When this procedure is applied to electromagnetic, weak and strong forces within the framework of SM, then these forces become more and more similar but they do not unify at any energy scale. However, when this study is repeated within the framework of supersymmetric standard model, then these forces are unified at an energy scale of $\sim 10^{16}$ GeV as shown in Figure 2.1. Here α_1^{-1}, α_2^{-1}, α_3^{-1} correspond to the gauge couplings for electromagnetic, weak and strong forces respectively. The unification of these forces is an important achievement as it indicates the unification energy of the GUT.

2.2.2 The Minimal Supersymmetric Standard Model (MSSM)

The Minimal Supersymmetric Standard Model (MSSM) [16], [17] is a supersymmetric extension of the SM with the addition of a minimal number of new particles. A SUSY transformation changes a fermionic state into a bosonic state and vice versa [15]

$$Q\,|\mathrm{Fermion}> \;=\; |\mathrm{Boson}>, \qquad Q\,|\mathrm{Boson}> \;=\; |\mathrm{Fermion}>, \tag{2.4}$$

where Q is an operator that gives such a transformation. The result of this transformation is a production of new particles called supersymmetric particles (or sparticles). SUSY postulates that for each SM particle, there exists a supersymmetric partner with identical quantum numbers except the spin which differs by half a unit. The sparticles predicted by the MSSM are given in Table 2.4. The symbol for superpartner is written with a tilde. The naming convention is to add a prefix s for the superpartner of a SM

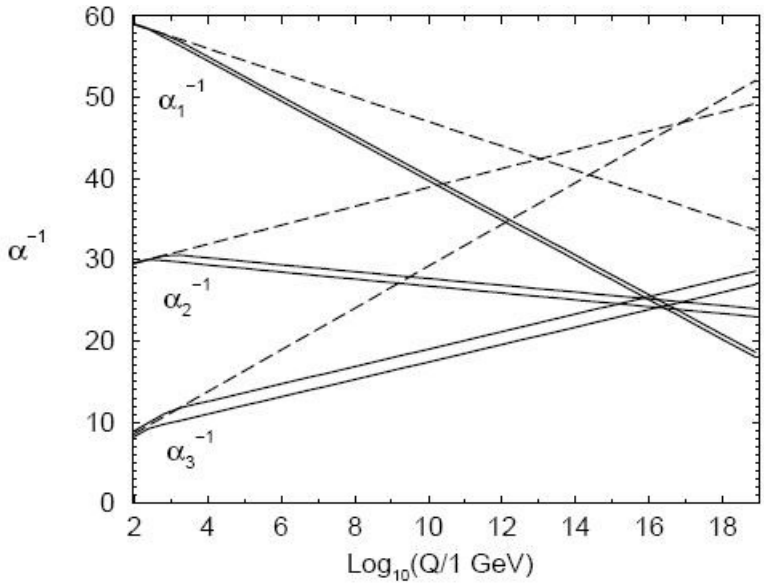

Figure 2.1: The running of the inverse gauge couplings α^{-1} with increasing interaction energy scale Q. The dashed lines represent the SM prediction while the solid lines are the predictions within the framework of supersymmetric SM [15].

fermion e.g. selectron ($\tilde{e}$), and to add the suffix *ino* for the superpartner of a SM boson e.g. gluino ($\tilde{g}$).

In the Standard Model only one Higgs field is needed to give masses to the particles. However, the MSSM requires two Higgs fields and it predicts five Higgs bosons: h^o, H^o, A^o, H^+ and H^-. These particles have the following superpartners: $\tilde{h^o}$, $\tilde{H^o}$, $\tilde{A^o}$, $\tilde{H^+}$ and $\tilde{H^-}$. The linear combination of $\tilde{h^o}$ and $\tilde{H^o}$ along with $\tilde{Z}$ and $\tilde{\gamma}$ define a set of four new

SM particles	SUSY partners	Spin of SUSY partners
quarks	squarks $\tilde{q}$	0
leptons	sleptons $\tilde{\ell}$	0
gluon	gluino $\tilde{g}$	$\frac{1}{2}$
$W^{\pm}$, $H^{\pm}$-field	charginos $\tilde{\chi}^{\pm}_{1,2}$	$\frac{1}{2}$
Z, γ, H-field	neutralinos $\tilde{\chi}^{0}_{1,2,3,4}$	$\frac{1}{2}$

Table 2.4: SM particles and their supersymmetric partners in the MSSM [12].

particle states $\tilde{\chi}_1^0$, $\tilde{\chi}_2^0$, $\tilde{\chi}_3^0$, $\tilde{\chi}_4^0$ called neutralinos. Similarly, $\tilde{H^+}$ and $\tilde{H^-}$ mix with $\tilde{W^+}$ and $\tilde{W^-}$ to produce $\tilde{\chi}_1^\pm$, $\tilde{\chi}_2^\pm$ called charginos. All the neutralinos and the charginos are shown in the Table 2.4.

The supersymmetry we have discussed so far is an exact symmetry where the masses of particles and sparticles are equal. But there is no direct experimental evidence of any superpartner yet. Therefore, SUSY is assumed to be a broken symmetry that allows the masses of sparticles to be much larger than their SM partners. We will discuss about broken symmetry in Section 2.2.3.

R-Parity

R-parity is a muliplicative quantum number which takes opposite values for the Standard Model and Supersymmetric particles, which are +1 and -1 respectively. This can be defined as

$$R \;=\; (-1)^{3(B-L)\,+\,2S}, \tag{2.5}$$

where B is the baryon number, L is the lepton number and S is a particle spin. There are two consequences of R-parity conservation. First, the sparticles are produced in pairs. Secondly, the lightest supersymmetric particle (LSP), to which all sparticles eventually decay, must be stable. In the MSSM, R-parity conservation is assumed.

2.2.3 The Minimal Supergravity Model (mSUGRA)

It has been mentioned in the previous section that SUSY is not an exact symmetry. The precise mechanism of broken symmetry is unknown but various models exist that attempt to describe SUSY breaking. The most popular among them is the Minimal Supergravity Model (mSUGRA) which is the special case of the MSSM. This model assumes that gravity is responsible for the mediation of symmetry breaking [18]. In defining the SUSY breaking mechanism, the mSUGRA model reduces the large number

Benchmark Points	m_o (GeV)	$m_{\frac{1}{2}}$ (GeV)	A_o (GeV)	$tan\beta$	$sign(\mu)$
SU1	70	350	0	10	+
SU2	3550	300	0	10	+
SU3	100	300	-300	6	+
SU4	200	160	-400	10	+
SU6	320	375	0	50	+
SU8.1	210	360	0	40	+

Table 2.5: Benchmark points in mSUGRA parameter space analysed by ATLAS [19].

of free parameters associated with the MSSM, which is more than 100, to a manageable number of five after imposing GUT conditions [18]. The following are the five parameters of mSUGRA:

$$m_o,\ m_{\frac{1}{2}},\ A_o,\ \tan\beta \ \text{ and } \ \text{sign}(\mu)$$

Here, m_o is the mass of all scalar particles at GUT scale, $m_{\frac{1}{2}}$ is the mass of all gauginos at GUT scale, A_o stands for the common trilinear Higgs-sfermion-sfermion coupling at the GUT scale, $\tan\beta$ is the ratio of vacuum expectation values of two Higgs fields and $\text{sign}(\mu)$ is the sign of Higgsino mass term.

Usually, different points in mSUGRA parameter space are chosen to study the various possible signatures which might face the experiment. The benchmark points studied by the ATLAS Experiment (topic of the next chapter) are listed in Table 2.5 [19]. The benchmark point SU4 is important to study as it could provide early SUSY discovery at the ATLAS Experiment. The sparticle mass hierarchy at SU4 is shown in Figure 2.2, and the masses of these sparticles are listed in Table 2.6 [20].

In mSUGRA model, the LSP is the lightest neutralino $\tilde{\chi}_1^0$ which is stable, massive and weakly interacting particle, and therefore this is an excellent candidate for the universe cold dark matter. The benchmark points listed in Table 2.5 are roughly consistent with the observed dark matter density [19].

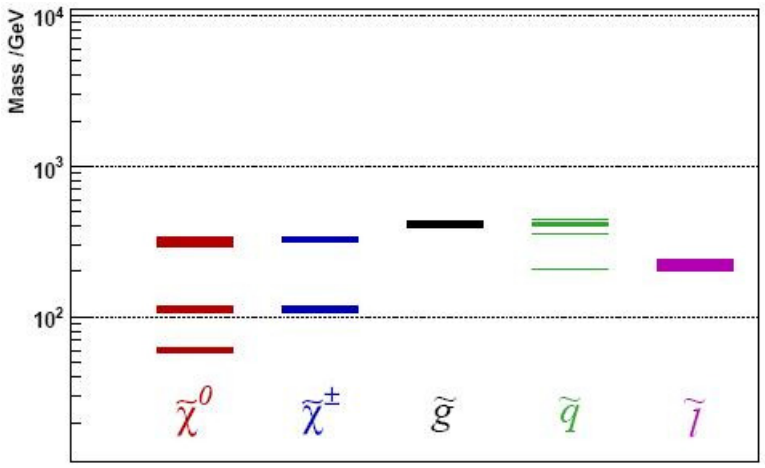

Figure 2.2: SU4 sparticle mass hierarchy (from Isajet 7.71) [20].

	Mass (GeV)		Mass (GeV)
$\tilde{g}$	413		
$\tilde{u_L}$	412	$\tilde{u_R}$	405
$\tilde{d_L}$	420	$\tilde{d_R}$	406
$\tilde{b_1}$	358	$\tilde{b_2}$	399
$\tilde{t_1}$	206	$\tilde{t_2}$	445
$\tilde{\ell_L}$	232	$\tilde{\ell_R}$	213
$\tilde{\tau_1}$	201	$\tilde{\tau_2}$	236
$\tilde{\nu_L}$	218	$\tilde{\nu_\tau}$	216
$\tilde{\chi}_1^0$	60	$\tilde{\chi}_2^0$	113
$\tilde{\chi}_3^0$	309	$\tilde{\chi}_4^0$	328
$\tilde{\chi}_1^\pm$	113	$\tilde{\chi}_2^\pm$	327

Table 2.6: SU4 sparticle masses (from Isajet 7.71), where $m_{\tilde{u}} \sim m_{\tilde{c}}$, $m_{\tilde{d}} \sim m_{\tilde{s}}$, $m_{\tilde{e}} \sim m_{\tilde{\mu}} = m_{\tilde{\ell}}$ and $m_{\tilde{\nu_e}} \sim m_{\tilde{\nu_\mu}} = m_{\tilde{\nu_L}}$ [20].

Chapter 3

The ATLAS Experiment

The previous chapter served to define the particle content and interactions of the Standard Model. It is also pointed out that the Supersymmetry is a possible extension to the SM which predicts new particles but none of them has been observed. In this chapter, the plan is to discuss how the fundamental particles of the SM are detected and their kinematic properties measured in ATLAS experiment. Here, a brief overview of the ATLAS detector is provided, more detailed information can be found in [21], [22]. Before opening the discussion on the ATLAS experiment, we take a quick look on the machine (Large Hadron Collider) which is designed to produce those particles that are mentioned in the previous chapter.

3.1 The Large Hadron Collider (LHC)

The Large Hadron Collider (LHC) is the world's highest energy accelerator which is situated at the European Organisation for Nuclear Research (CERN), Switzerland. It is a proton-proton collider which is contained in a circular tunnel with a circumference of 27 km. There are two counter-rotating proton beams, for which the design energy is 7 TeV each, which are collided at four different locations with a centre-of-mass energy

Machine Parameter	Value
Design beam energy at collision	7.0 TeV
Design luminosity	$10^{34}\ cm^{-2}\ s^{-1}$
Number of protons per bunch	1.05x10^{11}
Number of bunches per beam	2835
Time between bunches	25 ns
Frequency of bunch crossing	40 MHz
Number of events per bunch crossing	20
Beam life time	22 h
Crossing angle	200 μ rad
Injection energy	450 GeV
Dipole magnetic field	8.4 T
Circulating current per beam	0.53 A
r.m.s. beam radius at intersection point	16 μm

Table 3.1: LHC machine parameters (from [23]).

of 14 TeV. Some parameters of the LHC machine are listed in Table 3.1. In each beam, protons are grouped into bunches (or train) and each bunch carries $\sim 10^{11}$ protons. These bunches cross each collision point every 25 ns. Each point of proton-proton collision is studied by a detector. Four such detectors are ATLAS, CMS, ALICE and LHCb which are shown in Figure 3.1. The ATLAS and CMS are general purpose detectors while other two are special purpose. As this thesis is based on the ATLAS detector therefore, the discussion is solely focused on this experiment.

The LHC started its first operation on 10 September 2008 when it successfully circulated proton beams in both directions inside the main accelerator ring. On 30 March 2010, the LHC became the world's highest energy accelerator when the collisions took place at 7 TeV centre-of-mass energy. It is decided to continue operating with 7 TeV for few years and then the LHC will operate at the design energy of 14 TeV.

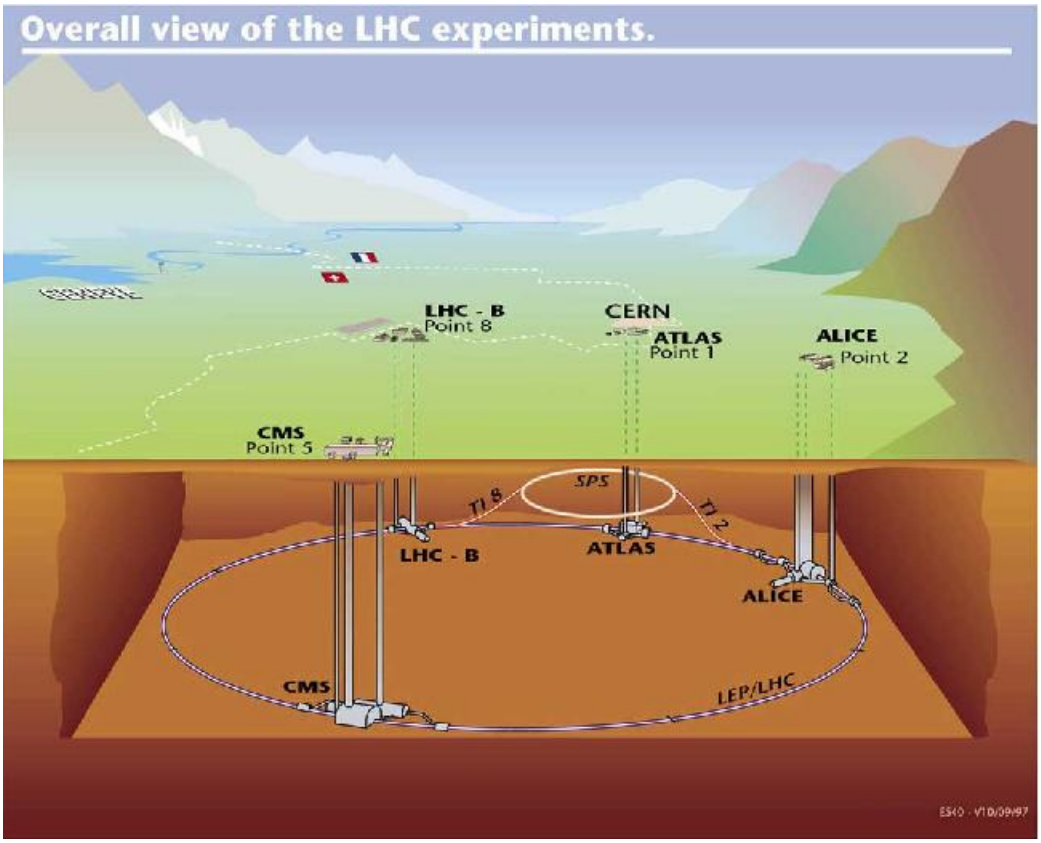

Figure 3.1: A sketch of the LHC along with four experiments [24]

3.2 A Toroidal LHC Apparatus (ATLAS)

A Toroidal LHC Apparatus (ATLAS) [21], [22] is a general purpose detector which has been placed at one of the collision points of the LHC. It detects and measures the properties of particles that are coming out from the production point. Usually, the general purpose detectors are designed to investigate several things: accuracy enhancement of known physics, confirmation of predicted particles, and searches of new phenomena. In this connection, the main goals of the ATLAS include the following: to explore physics at the TeV scale, to discover the Higgs boson, and to look for evidence of physics beyond the Standard Model, such as Supersymmetry. Like other general purpose detectors, the ATLAS is broken into various subsystems. It consists of a series of concentric cylinders around the interaction point where the proton beams collide. The major subsystems are the inner detector, calorimeters and muon spectrometers as shown in Figure 3.2. The performance goals of these subsystems are shown in Table 3.2. Each of these subsystems is further divided into multiple layers. The next few sections are devoted to a discussion of these subsystems.

The coordinate system of ATLAS is a right-handed system which has the following nomenclature: the interaction point is defined as the origin, the z-axis represents the beam axis, the x-axis pointing towards the centre of the LHC ring, and the y-axis describes the upward direction. Thus, the x-y plane is transverse to the beam axis. The polar angle θ is measured from the z-axis while the azimuthal angle ϕ is measured from the x-axis around the beam pipe. An important quantity that describes the angle of particle to the beam axis is called pseudorapidity (η) which is defined as

$$\eta = -\ln[\tan(\frac{\theta}{2})]. \tag{3.1}$$

The particles having larger values of $|\eta|$ are closer to the beam pipe, while the particles with a larger angles from the beam axis have lower $|\eta|$ values, and they are described

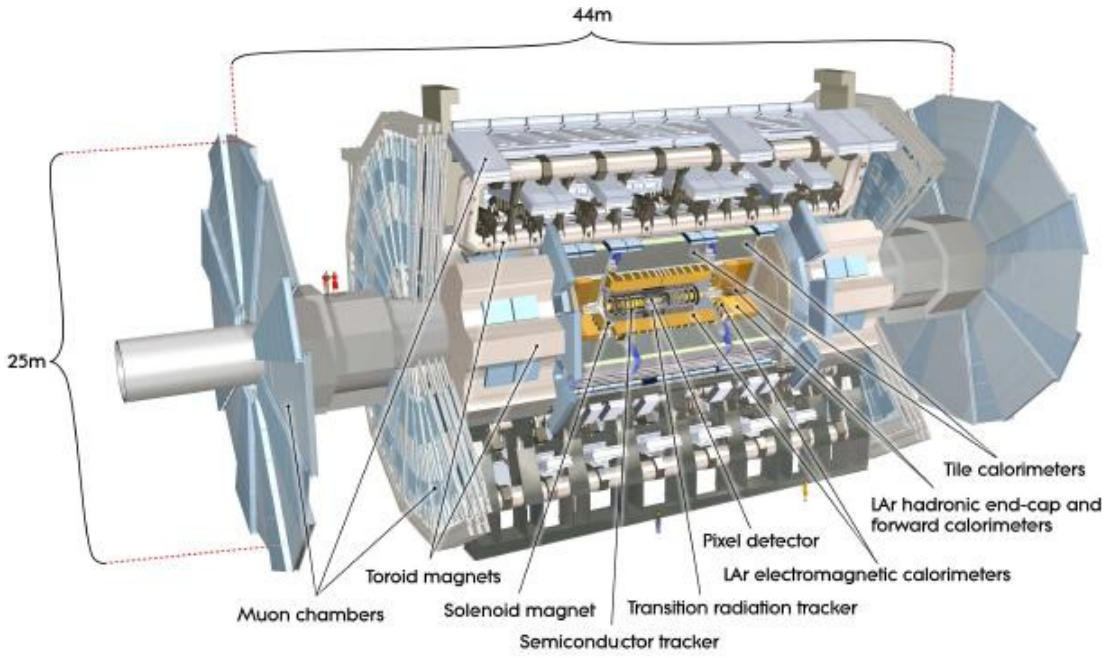

Figure 3.2: Cut-away view of the ATLAS detector [21].

as forward and central (or barrel) respectively. The ATLAS detector covers a pseudo-rapidity range of $|\eta| < 5$. Another useful quantity is a distance $\triangle R$ which is defined in the pseudorapidity - azimuthal angle space as

$$\triangle R = \sqrt{(\triangle\eta)^2 + (\triangle\phi)^2} \, . \tag{3.2}$$

In the LHC, the total momentum of the initial state is unknown. This is because the proton is not a fundamental particle instead it has constituents called partons (a collective name of quarks and gluons) which actually take part in the collision. Each parton takes a random share of the proton's momentum, as determined by a parton density function [25]. Due to the complicated nature of collisions in the hadron colliders, the measurements along the z-axis are not very useful because an unknown fraction of the energy escapes at low angles relative to the beam pipe. Therefore, momentum and energy are usually quoted in the transverse (x-y) plane. The transverse momentum (p_T)

Detector component	Required resolution (GeV)	$\lvert\eta\rvert$ coverage
Tracking	$\frac{\sigma_{p_T}}{p_T} = 0.05\%\ p_T \oplus 1\%$	< 2.5
EM calorimetry	$\frac{\sigma_E}{E} = \frac{10\%}{\sqrt{E}} \oplus 0.7\%$	< 3.2
Hadronic calorimetry		
barrel and end-cap	$\frac{\sigma_E}{E} = \frac{50\%}{\sqrt{E}} \oplus 3\%$	< 3.2
forward	$\frac{\sigma_E}{E} = \frac{100\%}{\sqrt{E}} \oplus 10\%$	3.1 - 4.9
Muon spectrometer	$\frac{\sigma_{p_T}}{p_T} = 10\%\ \ at\ \ p_T = 1\ TeV$	< 2.7

Table 3.2: Performance goals of the ATLAS detector [21], where $\oplus$ indicates addition in quadrature.

and transverse energy (E_T) are defined respectively as

$$p_T = \sqrt{p_x^2 + p_y^2}\,, \ \text{ and} \tag{3.3}$$

$$E_T = \sqrt{E_x^2 + E_y^2}\,, \tag{3.4}$$

where x, y are the momentum and energy components along these axes. However, the transverse momentum of the initial state is known which is zero, and the transverse momentum of particles in the final state can be measured. Any mismatch between the initial and final state momenta is usually quoted in terms of the missing transverse energy (E_T^{miss}) which indicates the presence of neutrino or other only weakly interacting particles such as the lightest neutralino ($\tilde{\chi}_1^0$).

3.2.1 Inner Detector

Inner detector (or inner tracker) is a collection of sensors arranged to measure the paths of charged particles as they move away from the collision point. The inner tracker consists of three independent but complementary sub-detectors. These sub-detectors

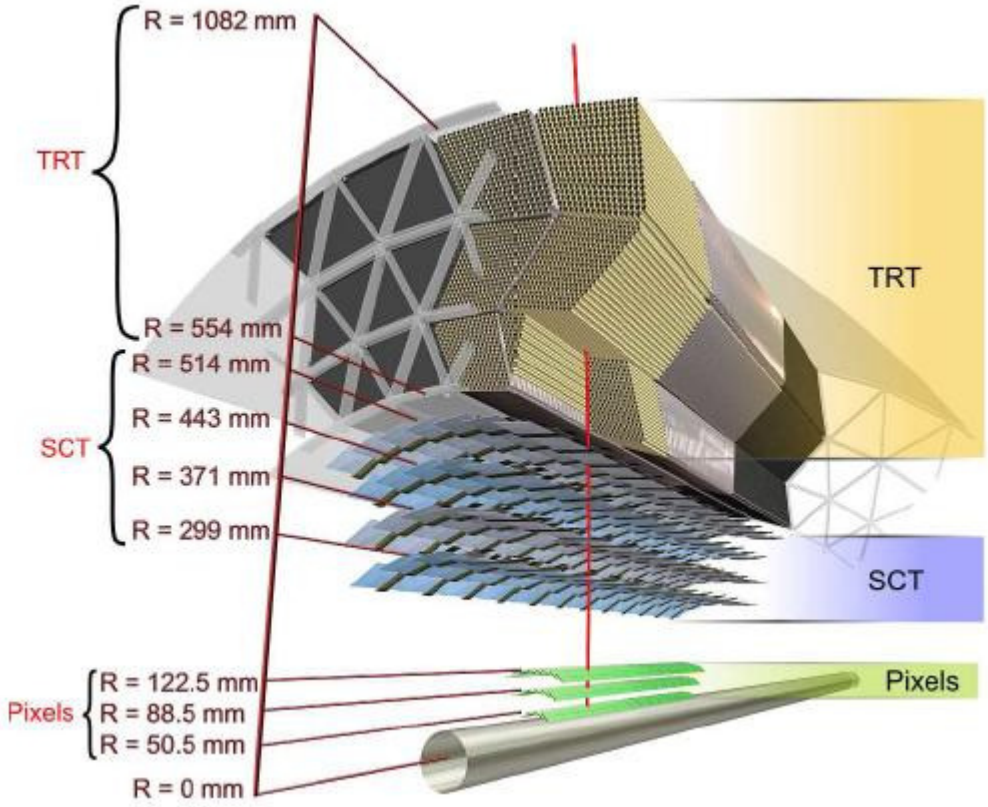

Figure 3.3: Three sub-detectors of the ATLAS inner tracker [21].

are the pixel detector, silicon-microstrip sensors (SCT), and transition radiation tracker (TRT) as shown in Figure 3.3. The entire inner detector is inside a magnet called the central solenoid. The solenoid provides a 2 T axial magnetic field for the inner tracker. The magnetic field causes the charged particles to curve when they emerge from the production point (or production vertex). The measurement of these curvatures result in the determination of particle's charge, position and momentum vector. The requirements imposed on the tracker are the following: accurate measurements of high p_T tracks, location of primary vertices, and identification of secondary vertices.

The accuracy of momentum measurement is defined by the resolution of tracking detectors in the magnetic field. The tracking resolution is determined by

$$\frac{\sigma_p}{p} = cp \oplus d, \tag{3.5}$$

where p is the particle's momentum, c is the error in measuring the bend angle of particle in the magnetic field, and d is a term due to multiple scattering which is only important at low particle's momentum. The tracking resolution required by the ATLAS detector is

$$\frac{\sigma_{p_T}}{p_T} = 0.05\%\ p_T \oplus 1\%. \tag{3.6}$$

Pixel Detector

The pixel detector is the innermost part of the detector which is comprised of three cylindrical layers in the barrel, and three disk layers in each of the two end-caps. The detecting material is made of silicon with a thickness of 250 μm. The smallest unit that can be read out is a pixel which has a size of 50 x 400 μm^2. When a pixel is traversed by a charged particle, it produces a signal and provides a position measurement. There are 1744 modules in total, each measuring 2 cm by 6 cm. Each module contains 16 readout chips and other electronic components. There are roughly 47,000 pixels per module. The minute pixel size is designed for precise track measurement very close to the interaction point. Due to its high granularity, the pixel detector has low hit occupancy which is very important for pattern recognition. The position accuracy of the pixel detector is 10 microns [26].

Silicon-Microstrip Sensors (SCT)

The middle component of the inner detector is the Silicon-Microstrip Sensors (SCT). The SCT is similar in function to the pixel detector but instead of small pixels, it has a long, narrow strips. It is composed of four double layers of silicon strips as shown in Figure 3.3. Each strip measures 80 μm by 12.6 cm. In order to measure the particle tracks, the SCT

covers a much larger area and more sample points than the pixel detector. The position accuracy of SCT is few tens of microns [26].

Transition Radiation Tracker (TRT)

The outermost component of the inner detector is the transition radiation tracker (TRT). Here, the detecting elements are gas filled straws (or drift tubes) as shown in Figure 3.3. Each straw is 4 mm in diameter with a length of up to 144 cm. The gas inside the straw becomes ionized when a charged particle passes through. The charge is then converted into signal that results in the measurement of particle's position. The position accuracy of TRT is about 200 microns [26].

Moreover, the transition radiation tracker also takes part in the identification of electrons. The electron identification capability is added by employing Xenon gas to detect transition radiation photon created in a radiator between straws.

3.2.2 Calorimeters

After the tracker, particles encounter the calorimeter system as shown in Figure 3.4. The calorimeters are situated outside the solenoid magnet that surrounds the inner detector. The purpose of the calorimeter are to measure a particle's energy by absorbing it. The calorimeters are designed to provide large solid angle coverage, fine segmentation and good energy resolution. The ATLAS calorimeter covers a range of $|\eta| < 4.9$. The energy resolution of calorimeter can be expressed as

$$\frac{\sigma_E}{E} = \frac{a}{\sqrt{E}} \oplus b, \tag{3.7}$$

where E is the particle energy, a is the statistical fluctuations in the sampled energy, and b is the non-uniformity of the medium. The above relation represents that precision improves with particle energy, which is in contrast to the tracking resolution (Equation 3.5) where the precision downgrades with rise in energy.

The calorimeters are sub-divided into the electromagnetic calorimeter (ECAL) and the hadronic calorimeter (HCAL). The inner calorimeter is the ECAL while HCAL is the outer calorimeter.

Electromagnetic Calorimeter (ECAL)

The electromagnetic calorimeter (ECAL) absorbs and measures the energies of electrons and photons produced in the collision. The identification of and accurate reconstruction of these particles are the required capabilities of ECAL. The energy resolution of ECAL in ATLAS is given by

$$\frac{\sigma_E}{E} = \frac{10\%}{\sqrt{E}} \oplus 0.7\%. \tag{3.8}$$

The ECAL consists of many layers of lead plates with liquid argon as a sampling material. The function of the lead plates is to absorb the incident particle, and transform its energy into a shower of lower energy particles. When the shower particles traverse the argon, between the plates, they create ionization. The ionization results in the production of electronic signal which is proportional to the incident particle energy. There are two radiative processes that initiate the above electromagnetic shower. They are Bremsstrahlung radiation produced by electron, and pair-production of electron-positron produced by photon. There is a characteristic length scale associated with these radiative processes in the material called the radiation length (X_o). The thickness of ECAL is usually quoted in terms of radiation lengths. The total thickness of ECAL in ATLAS is over $22\,X_o$ in the barrel and over $24\,X_o$ in the end caps.

Hadronic Calorimeter (HCAL)

The hadronic calorimeter (HCAL) surrounds the electromagnetic calorimeter, and like ECAL, it is also a sampling calorimeter. The HCAL absorbs and measures the energies of hadronic jets. The hadronic jets are a group of high energy hadrons (e.g. pions, kaons,

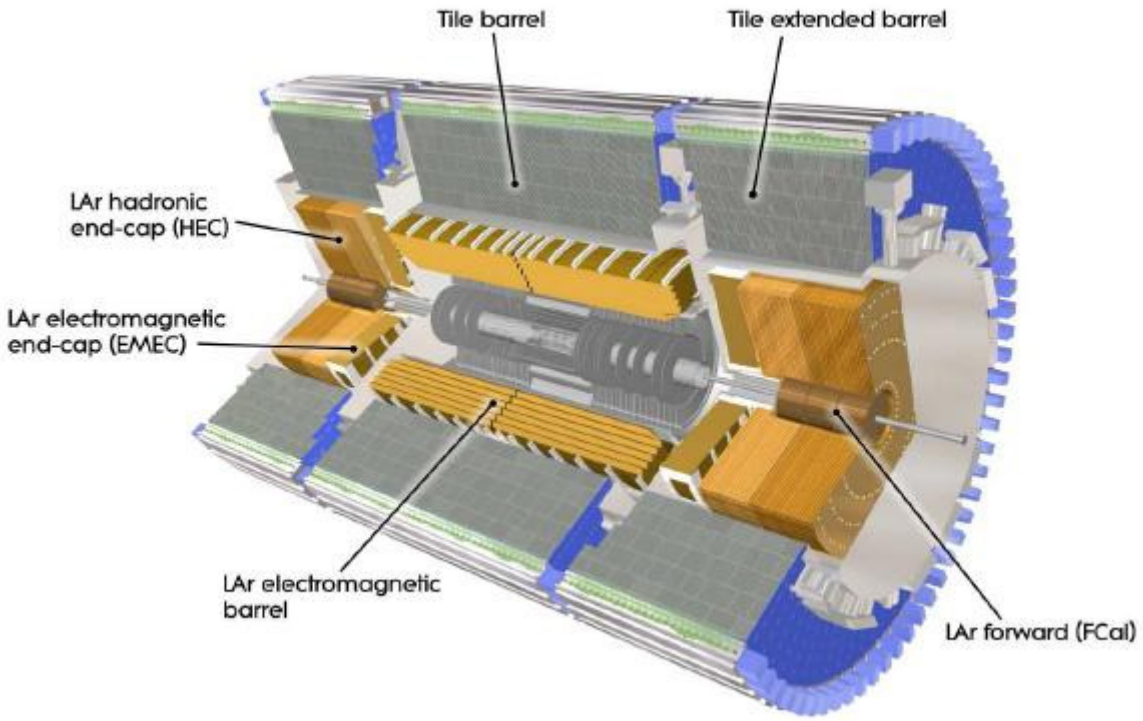

Figure 3.4: Cut-away view of the ATLAS calorimeter system [21].

protons) that move in a narrow cone. Besides identification and energy measurement of the hadronic jets, the major goal of HCAL is to measure the missing transverse energy (E_T^{miss}) [Ref]. The energy resolution of HCAL in the barrel and end-cap region is given by

$$\frac{\sigma_E}{E} = \frac{50\%}{\sqrt{E}} \oplus 3\%. \tag{3.9}$$

The HCAL consists of steel plates separated by plastic tiles or scintillators. The function of the steel plates is to absorb the jet particles and transform their energies into a shower of lower energy hadrons. When the shower particles interact with plastic tiles, they produce scintillations. The amount of light emitted by the scintillator is proportional to the incident energy of jet particles. There is a characteristic length scale in the medium, called the the interaction length λ (mean free path), at which a hadronic interaction occurs. In ATLAS, the approximate thickness is $9.7\,\lambda$ in the barrel and $10\,\lambda$ in the end caps.

3.2.3 Muon Spectrometer

The final layer of sub-detector system, outside HCAL, is the muon spectrometer. It is designed to identify muons and measure their momentum in the range $|\eta| < 2.7$. Its layout is shown in Figure 3.5. The muons are very penetrating and they are the only charged particles which are not absorbed by the calorimeter. Therefore, particles that are observed in the muon spectrometer are assumed to be muons. Its function is similar to the inner tracking system i.e. it constructs particle curvature in the magnetic field and measures its momentum. But instead of a solenoid, the magnetic field is provided by three toroids, one barrel and two end-cap toroids, with a field strength of 0.5 T and 1 T respectively. These toroids along with the central solenoid are shown in Figure 3.6. The resolution of muon spectrometer required by ATLAS is

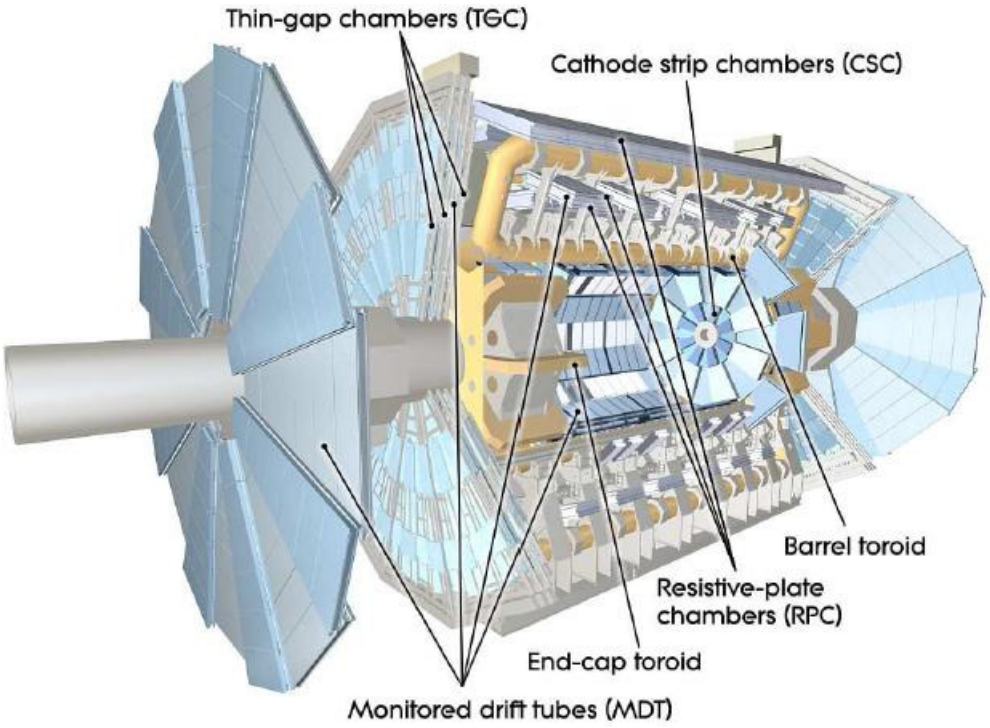

Figure 3.5: Cut-away view of the ATLAS muon system [21].

$$\frac{\sigma_{p_T}}{p_T} = 10\% \;\; at \;\; p_T = 1 \; TeV \tag{3.10}$$

Most of the $|\eta|$ range is covered by muon sensors called muon drift tubes (MDT). These are gas-filled metal tubes, 3 cm in diameter, with high voltage wires running on their axes. When muons pass through these tubes, they produce electrical pulses in the wires. These pulses allow position measurement to 0.1 mm. At large pseudorapidities, muon drift tubes are not suitable for muon measurements because of high radiation environment. Therefore, cathod strip chambers (CSC) are used instead. Cathod strip chambers are multiwire proportional chambers with cathode segmented into strips. The muons traverse the chambers produce signals that allow position measurement to 0.1 mm.

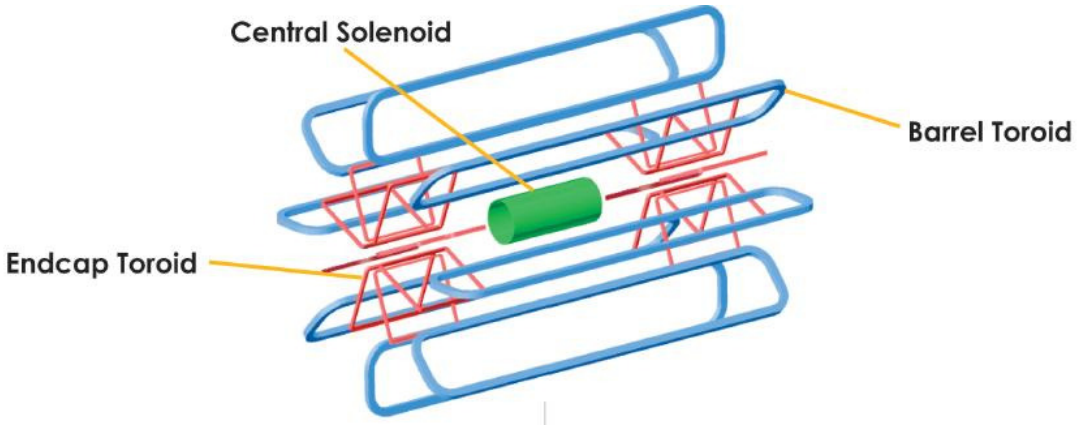

Figure 3.6: A solenoid, a barrel toroid and two end-cap toroids of the ATLAS magnet system [23].

3.2.4 The Trigger System

It is pointed out in Table 3.1 that the LHC has a designed luminosity of 10^{34} cm^{-2} s^{-1} with a bunch crossing of 25 ns. At this level, the interaction rate will be about 10^9 Hz. Out of these interactions, only a few are expected to have special characteristics that might lead to new discoveries. Therefore, in order to avoid storing immense amount of uninteresting information, only those events are selected for storage that have special characteristics. This selection is a highly delicate procedure which is carried out by the *trigger*. The trigger system in ATLAS has three distinct levels: level-1 (L1), level-2 (L2) and event filter (EF). Further, L2 and EF are collectively known as high level trigger (HLT) as shown in Figure 3.7. The ATLAS trigger system reduces the huge interaction rate of 10^9 Hz to $\sim 10^2$ Hz, i.e., a rejection factor of 10^7.

Level-1 is a hardware trigger which is based on the coarse calorimeter and muon information. It searches for high transverse momentum electrons, muons, photons and jets, as well as for the missing transverse energy and total transverse energy. In each event, it also defines one or more Regions-of-Interest (RoIs) i.e. those regions where its selection process identifies interesting features. Level-1 trigger makes a decision in less than 2.5 μs and reduces the interaction rate to about 75 kHz. After L1 trigger, the next

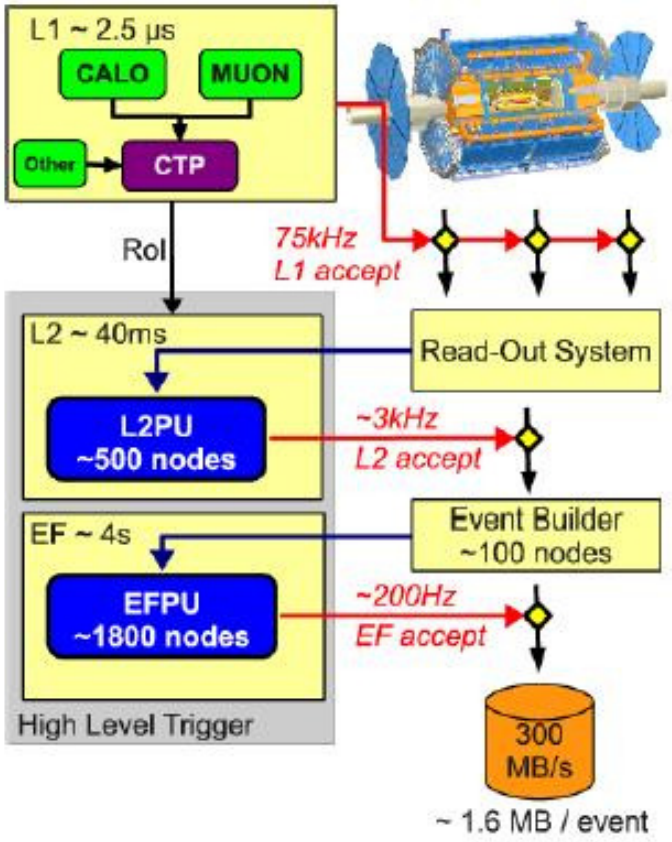

Figure 3.7: The ATLAS trigger with design specifications of the interaction rates [27].

stage is level-2 which is a software trigger. L2 trigger uses all the available data within the RoI's. It is designed to reduce the interaction rate to about 3 kHz with an event processing time of ~ 40 ms. The final stage of the event selection process is carried out by the event filter which is also a software trigger. It performs a detailed analysis on the full event data. The EF is designed to reduce the interaction rate to about 200 Hz with an event processing time of ~ 4 s. If the event is accepted, the data is sent to the storage system. About one petabyte (one million gigabytes) of data is expected to be recorded each year.

Chapter 4

Event Simulation and Particle Reconstruction in ATLAS

The previous chapter served to describe how the particles are detected and their kinematic properties measured in the ATLAS detector. In this chapter, our aim is to provide an overview of event simulation and reconstruction of particles in ATLAS. At first, the simulation process is discussed, in which various stages are involved to produce data in a format that can be used for physics analysis. Later we describe reconstruction of physical objects in ATLAS. Here, our discussion will be focused on electrons, muons, jets and missing transverse energy. These objects are defined on the basis of the criteria recommended by ATLAS for Computing System Challenge (CSC) exercise [19]. Excellent identification capability of these objects is needed for most physics studies carried out at the LHC, including searches for Supersymmetry.

Here, we will only provide a brief overview of the simulation and reconstruction of particles in ATLAS. The main reference for this chapter is [19], [28] where one can find the full details.

4.1 Event Simulation

Event simulations are used to generate particle physics events and simulate the response of a detector expected as a result of these events. These computer simulations are based on Monte Carlo MC methods. The Monte Carlo method uses random number generator to model the physics processes and the interactions of the particles with the detector. The simulation process is composed of various stages as shown in Figure 4.1.

The first stage is the event generator. This is a Monte Carlo program which simulates particle physics events with probabilities as predicted by a given theory. In general, there are two classes of event generator programs: general purpose and specialised. The general purpose generator does everything starting from proton-proton initial state to the final state particles, while the specialised generators just describe part of the process and provide improved descriptions of specific decays or final states.

For example, PYTHIA [29] is a general purpose program which can simulate high energy physics events in various combinations. In PYTHIA, a typical high energy event may be described as: Two particle beams (e.g protons) come towards each other. Each particle in the beam is characterised by a parton density function, which describes the partonic substructure in terms of flavour composition and energy sharing. A shower initiator parton from each beam starts off a sequence of branchings such as $q \rightarrow qg$ to build up an initial-state shower. One incoming parton from each of the two showers enters the hard process, which results in the production of outgoing partons (usually two). The outgoing parton may branch to build a final-state shower.

When a shower initiator is taken out of a beam particle, a beam remnant is left behind. This remnant may have an internal structure, and a net colour charge that relates it to the rest of the final state. With each branching, the QCD force grows until the confinement mechanism groups the partons together in to colour neutral hadrons. Many of the produced hadrons are unstable and decay further.

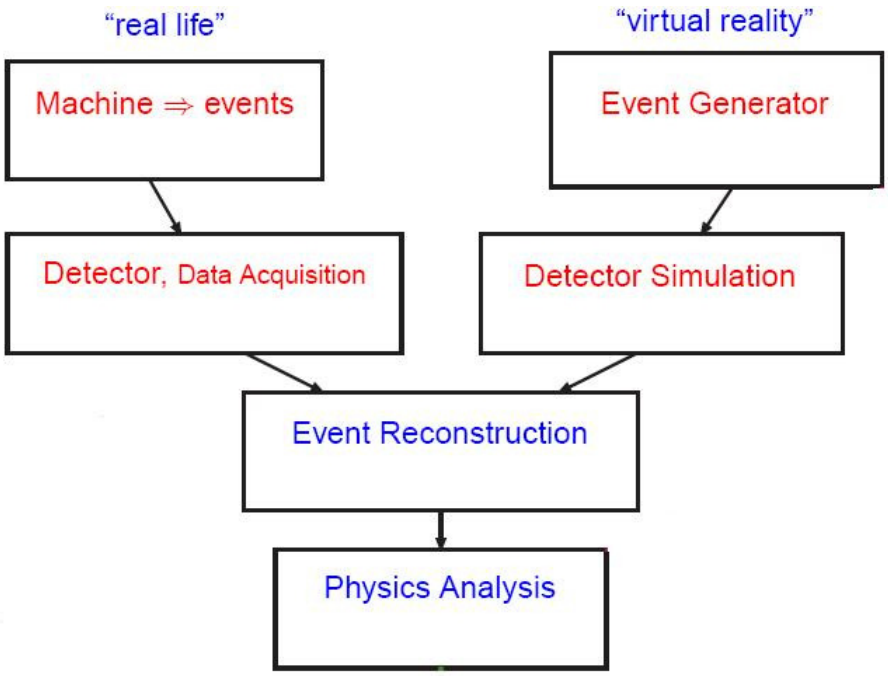

Figure 4.1: Major stages in the production of simulated and real data [30].

Finally, the event generator programs provide total cross-section for a particular process. In addition to this, they also deliver four-vectors of momenta of particles produced as a result of proton-proton collision. Full details of the above description can be found in [29].

Next one needs to know how the detector will respond to those particles. At this stage, Monte Carlo detector simulation comes into picture. The detector simulation is achieved by a detailed modelling of particle interactions with the detector medium (full simulation) using a program based on the GEANT4 package [31]. This models the response of the detector and produces raw data which is in the same format as real data.

The full simulation process is very CPU intensive due to the detailed description of the detector. Therefore, if the physics studies require to simulate large samples of events, then one uses the fast simulation package, ATLFAST [32]. This replaces the full detector simulation and reconstruction phases of the Monte Carlo reconstruction

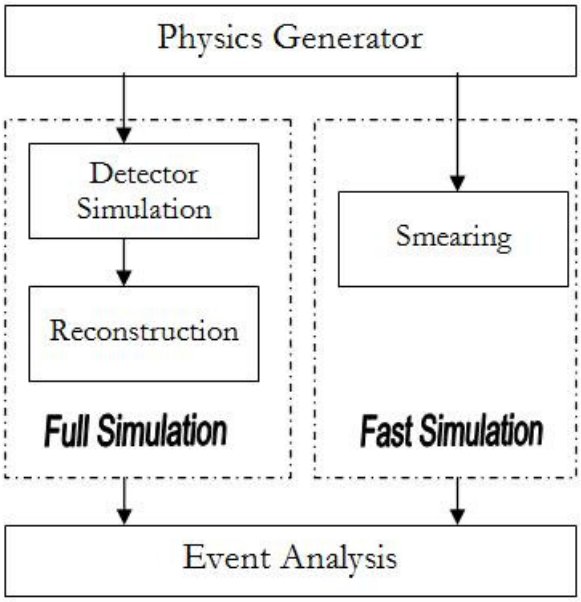

Figure 4.2: Full simulation versus ATLFAST simulation. Adapted from [33].

chain with appropriate smearing functions as shown in Figure 4.2. Since no detailed simulations of particle interactions are involved, therefore CPU time is reduced. The speed at which ATLFAST runs depends on many factors, e.g., complexity of physics channel, but in general, it is 4 or 5 orders of magnitude faster than running the full simulation chain [33]. Full details about ATLFAST package can be found in [33].

4.2 Particle Reconstruction

The role of reconstruction is to transform the stored raw data into the so called physics objects which are necessary for physics analysis. These objects correspond to the detector signals that are consistent with those expected as a result of particle interactions with the detector. The types of reconstructed objects include electrons, muons, and jets. Performance studies of these objects are not the aim of this section, but one can find these details in Ref [19]. The majority of the physics objects in ATLAS are composed from the tracks in the inner detector and muon spectrometer, and energy deposits (or

cluster) in the calorimeters.

Various algorithms are used for the reconstruction and identification of these objects. These algorithms are common for both simulated and real data. The format of data used here is *Analysis Object Data* AOD [28]. The reconstructed objects are grouped into containers. These objects are loosely reconstructed therefore, the same object may be reconstructed by two or more identification algorithms. Consequently, the same object may be present in more than one container e.g. an electron may be present in both electron and jet containers. In order to avoid the double counting of an object, overlap removal procedure is applied to the containers of the AOD.

4.2.1 Electrons

As electrons are charged particles, when they come out from the interaction point, they leave tracks in the inner detector. In addition to the tracks, they also deposit energy in the electromagnetic calorimeter. Therefore, reconstruction of electrons is performed using the information stored in both sub-detector systems. There are two main algorithms for electron reconstruction used in ATLAS. The details of the electron reconstruction algorithms can be found in Ref [19]. The first is the standard algorithm for isolated high p_T electrons which is seeded from the electromagnetic calorimeter. The second algorithm is for non-isolated low p_T electrons which is seeded from the inner detector. In this thesis, the standard algorithm is used for electron reconstruction. In the standard reconstruction of electrons, a cluster is found in the electromagnetic calorimeter using sliding window algorithm. The sliding window algorithm searches for the $\eta \times \phi$ window where the total energy is maximum. Following the identification of electromagnetic cluster, a matching track is searched in the inner detector.

4.2.2 Muons

As muons are very penetrating, they leave tracks both in the inner detector and muon spectrometer. In addition to the tracks, they also lose some energy in the calorimeters. Therefore, information from all sub-detector systems are used for the reconstruction of muons. ATLAS implements three ways to reconstruct muons, the details of muon algorithms can be found in Ref [19], [34]. One approach is to reconstruct standalone muons by finding tracks in the muon spectrometer alone. Another method is of combined muons in which muons are first identified as standalone and then matched with the track in the inner detector. The third is tagged muon approach in which muons are identified by extrapolating inner detector tracks to the track segments in the muon spectrometer.

4.2.3 Jets

A jet is a combination of information stored as tracks in the inner detector as well as energy deposited in the electromagnetic and hadronic calorimeters. Two different signals from the calorimeter are used for jet finding which are tower and topological clusters. Towers are formed by collecting cells into bins of $\triangle\eta \times \triangle\phi = 0.1 \times 0.1$ grid and summing up their energy deposits. Topological cell clusters represent an attempt to reconstruct three-dimensional energy deposition in the calorimeter. The reconstruction of jets in ATLAS is performed by various algorithms e.g. cone algorithm, k_t algorithm, Anti-k_t algorithm etc. The details of these algorithms can be found in [19], [35]. The cone jet algorithm is a collection of particles within a cone size $\triangle R = \sqrt{(\triangle\eta)^2 + (\triangle\phi)^2}$ of either 0.4 or 0.7. It takes transverse energy threshold of 1 GeV as a seed. The axis of the cone is aligned with the four-momentum of jet. The k_t algorithm adds jet constituents by working pair-wise grouping of closest objects. The distance parameter $R = \sqrt{(\triangle\eta)^2 + (\triangle\phi)^2}$ is adjusted to 0.4 and 0.6 for narrow and wide jets respectively. The Anti-k_t algorithm is similar to k_t algorithm except it groups highest p_T objects first instead of grouping closest objects first.

4.2.4 Missing Transverse Energy

The total transverse energy E_T of an event in ATLAS is measured by summing together the energy deposited in the calorimeter and muon systems in the transverse plane. The missing transverse energy is defined as the energy imbalance between the E_T and the total transverse energy of the colliding particles. The particles that interact only weakly such as neutrinos or the lightest neutralinos escape the detector medium without leaving any signal. Therefore, direct measurement of these particles is not possible instead their presence are inferred by measuring the missing transverse energy. In addition to these weakly interacting particles, there are other sources of missing transverse energy, called fake sources, such as instrumental effects, noisy or dead calorimeter cells, badly reconstructed or fake muons and acceptance effects due to lack of coverage over certain regions. Therefore, a very good measurement of the missing transverse energy is a critical requirement for the study of many physics channels in ATLAS including supersymmetry. The details of the determination of missing transverse energy in ATLAS can be found in [19].

Chapter 5

Dilepton SUSY Search

The previous three chapters served to provide a foundation that is needed to examine the production of supersymmetric particles in p-p collisions inside the ATLAS detector. In this chapter, our aim is to provide the analysis overview of the SUSY search based on the dilepton channel. The characteristic signatures of supersymmetry in the LHC are high momentum jets, large missing energy and a number of leptons (≥ 0). The search for these signatures is performed by looking for an excess of events in various SUSY channels including the dilepton channel. Many studies have been devoted to the dilepton channel inside the ATLAS collaboration. One official analysis at the centre-of-mass energy of 7 TeV has been done recently, which is the main Ref [1] of this chapter. The analysis described here takes the official dilepton analysis as a starting point, and here it is reviewed with slight modification.

5.1 The Dilepton Channel

This channel is characterised by the presence of two leptons in the final state, and this is a very promising venue for the discovery and measurement of Supersymmetry [1]. Many studies have been devoted to this signature in the last sixteen years. The two leptons

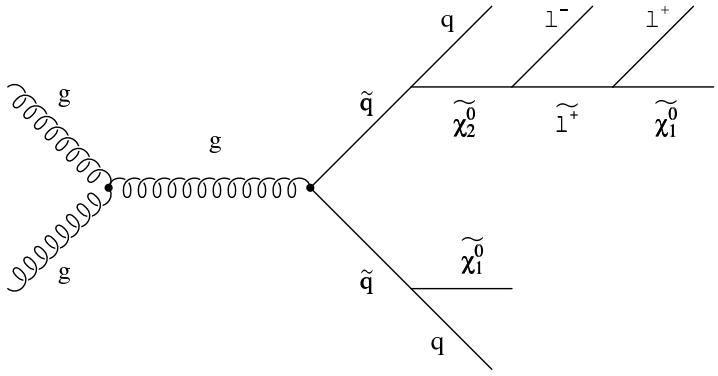

Figure 5.1: Feynman diagram of a signal process which contains two opposite sign leptons that are produced via $\tilde{\chi}_2^0$ decay.

in the final state can have either same or opposite sign. This study has been performed with opposite sign leptons.

If R-parity is conserved, two supersymmetric particles are produced in each SUSY event, each of which cascades to the lightest supersymmetric particle (LSP). The LSPs are a source of missing energy in the event. In the SUSY dilepton event, two opposite sign leptons (ℓ) can be produced in SUSY cascade through the decays of neutralinos ($\tilde{\chi}_i^0$) and charginos ($\tilde{\chi}_i^{\pm}$), e.g.

$$\tilde{\chi}_i^0 \longrightarrow \ell^{\pm}\ell^{\mp}\tilde{\chi}_j^0 \quad and \tag{5.1}$$

$$\tilde{\chi}_i^{\pm} \longrightarrow \ell^{\pm}\ell^{\mp}\tilde{\chi}_j^{\pm} \, . \tag{5.2}$$

Feynman diagrams of these processes are shown in Figures 5.1 and 5.2 respectively.

5.2 Analysis Overview

This SUSY dilepton study has been performed with fully simulated AODs (Section 4.2) at the centre-of-mass energy of 7 TeV by using ATLAS software called Athena [28]. The Monte Carlo samples we have used in this analysis are centrally produced within the

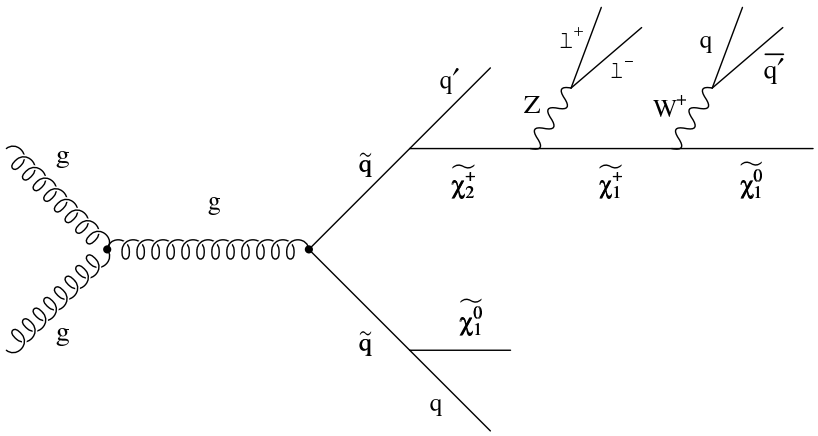

Figure 5.2: Feynman diagram of a signal process which contains two opposite sign leptons that are produced via $\tilde{\chi}_2^+$ decay.

ATLAS collaboration, and these are listed in Section 5.2.3.

5.2.1 Event Selection

In the SUSY dilepton search, the final state contains two leptons, two jets (at least) and missing transverse energy as shown in Figure 5.3. Here, the word lepton is used to denote isolated electrons and muons. Events are vetoed if the number of leptons are greater than two. This is done in order to avoid overlapping with a separate trilepton analysis being carried out in ATLAS that requires three leptons in the final state. Moreover, events are also vetoed if an electron is contained within the crack region, $1.37 < |\eta| < 1.52$, because of the degraded calorimeter coverage in this region. The basic selection criteria applied in this study are:

1. Two opposite sign leptons with $p_T^{lepton} > 20$ GeV and $|\eta| < 2.5$.

2. Two jets with $p_{T_1}^{jet} > 100$ GeV and $p_{T_2}^{jet} > 50$ GeV, and $|\eta| < 2.5$.

3. $E_T^{miss} > 80$ GeV and $E_T^{miss} > 0.3\, M_{eff}$.

4. $S_T > 0.2$.

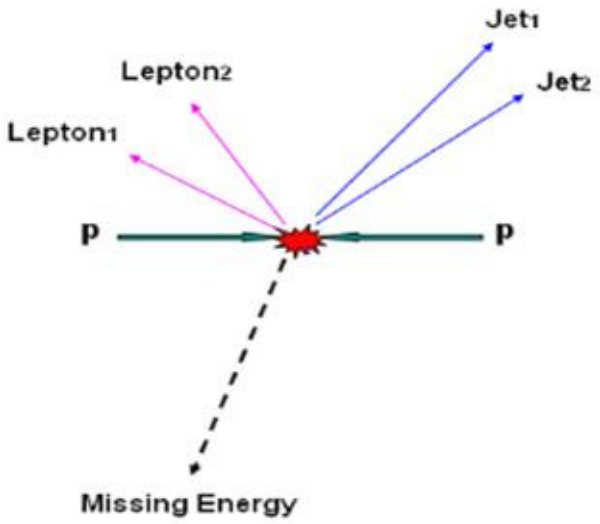

Figure 5.3: Schematic illustration of the final state of the SUSY dilepton mode.

Here p_T^{lepton}, $p_{T_1}^{jet}$ and $p_{T_2}^{jet}$ are the transverse momenta of the leptons, leading jet and next-to-the leading jet respectively. E_T^{miss} is the missing transverse energy of the event. M_{eff} is the effective mass which is the scalar sum of transverse momenta of all main objects, and is defined as

$$M_{eff} = \sum_{i=1}^{N_{jets}} p_T^{jet,i} + \sum_{i=1}^{N_{lep}} p_T^{lep,i} + E_T^{miss}, \tag{5.3}$$

where N_{jets} is the number of jets and N_{lep} is the number of leptons defining the analysis. S_T is the transverse sphericity and is defined as

$$S_T = \frac{2\,\lambda_2}{(\lambda_1 + \lambda_2)}\,, \tag{5.4}$$

where λ_1 and λ_2 are the eigenvalues of 2×2 sphericity tensor $S_{ij} = \sum_k p_{ki} p^{kj}$ computed from all selected jets and leptons. Here, λ_1 is assumed to be greater than λ_2. S_T is defined between 0 and 1 inclusive $0 \leq S_T \leq 1$, where '0' would correspond to a perfect back-to-back event and '1' to a completely isotropic one. The reason for considering this variable is that QCD di-jet events are expected to be back-to-back where as 'squark'

production events are not expected to be back-to-back (they are more spherical).

M_{eff} and S_T are the event shape variables. As the characteristic signatures of SUSY are high transverse momentum p_T of jets and large missing energy E_T^{miss}, therefore SUSY events are expected to have large values of M_{eff}. It means, a high cut on M_{eff} will further suppress non-SUSY events.

In this study, we have relaxed a cut on p_T of the leading jet (point 2 above), i.e., $p_{T_1}^{jet} > 100$ GeV. In the previous study, it was $p_{T_1}^{jet} > 180$ GeV which was necessary because of the large uncertainty in the $t\bar{t}$ background. In the present analysis, this uncertainty is substantially reduced by using a $t\bar{t}$ control sample from data. Therefore, here we can lower the $p_{T_1}^{jet}$ cut and obtain a higher signal efficiency. This technique for estimating the $t\bar{t}$ background is detailed in the next chapter.

5.2.2 Physics Object Definitions

The following object selection defines particle candidates which are used during event selection process. The object selection criteria are mostly based on official dilepton studies [1].

Electrons

Electron candidates are reconstructed by the algorithm called egamma. Electrons are also required to be isolated in the calorimeter, i.e., the total calorimeter energy within a cone of $\triangle R < 0.2$ (where $\triangle R = \sqrt{(\triangle\eta)^2 + (\triangle\phi)^2}$) should be less than 10 GeV. In addition to this standard cut, the p_T of electrons should be greater than 20 GeV and $|\eta|$ should be less than 2.5.

Muons

Muons are reconstructed by the algorithm called Staco muon. We take muon candidates that are combined tracks from the muon spectrometer and the inner tracker. In order to

select an isolated muon, the total calorimeter energy within a cone of $\triangle R < 0.2$ should be less than 10 GeV. Finally, the p_T of muons should be greater than 20 GeV and $|\eta|$ should be less than 2.5.

Jets

Jet candidates are reconstructed by the anti-k$_t$ jet algorithm with $\triangle R = 0.4$ based on tower clusters. The selected jets must have p_T greater than 20 GeV and $|\eta|$ should be less than 2.5.

Missing Transverse Energy

After calculations of the transverse energy, the resulting value is calibrated to get a more reliable number. Calibration of the energy can be done in different ways. One standard method is called the refined calibration where calorimeter cells are associated with an identified physics object. In this way, the reconstruction of missing transverse energy is improved, and more accurately corresponds to the energy carried away by non-interacting particles. One configuartion of refined calibration is MET-RefFinal [36], and this has been used in this analysis for the calculation of missing transverse enegy.

Overlap Removal

After passing the object selection criteria, it is expected that objects may overlap. For example, an electron could be reconstructed both as an electron and as a jet. When the candidate objects overlap with each other, a procedure is required to remove all overlapping objects except one. The overlapping criteria are based on the geometrical variable $\triangle R = \sqrt{(\triangle\eta)^2 + (\triangle\phi)^2}$ and is applied as follows:

1. if an electron and a jet are found within $\triangle R < 0.2$, keep the electron and remove the jet.

2. if a muon and a jet are found within $\triangle R < 0.4$, keep the jet and remove the muon.

3. if an electron and a jet are found within $0.2 \leq \triangle R < 0.4$, keep the jet and remove the electron.

5.2.3 SUSY Signal and SM Background Processes

In R-parity conserving models, two supersymmetric particles are produced in each SUSY event, each of which cascades to the lightest supersymmetric particle (LSP). As mentioned in Section 5.1, two opposite sign leptons can be produced in signal events via decays of neutralinos $\tilde{\chi}_i^0$ and charginos $\tilde{\chi}_i^{\pm}$ (Equations 5.1 and 5.2).

In Chapter 2, we mentioned a set of mSUGRA points that were considered during the ATLAS CSC excercise. In this thesis, the benchmark point SU4 is used which is defined by the following mSUGRA parameters: m_o = 200 GeV, $M_{\frac{1}{2}}$ = 160 GeV, A = -400 GeV, tanβ = 10 and $\mu > 0$. The Monte Carlo sample of SU4 used in the analysis is detailed in Table 5.1.

A variety of processes exist in the Standard Model that can produce two opposite sign leptons in the final state and will be regarded as background to a SUSY signal. The SM processes considered as background for the SUSY dilepton analysis are $t\bar{t}$, W+jets, Z+jets, diboson and Drell-Yan. The MC samples of these SM backgrounds are detailed in Table 5.1, Table 5.2 and Table 5.3. Further details on these MC samples are given in Appendix A.

After requiring two opposite sign leptons in the events of the above processes, several distributions are plotted as shown in Figures 5.4 to 5.7. These distributions are normalized to $1fb^{-1}$ of integrated luminosity. In these plots, Z+jets and $t\bar{t}$ backgrounds contributed significantly. When defining a signal region for the dilepton analysis, one begins by considering the dominant background to the search. It is clear from Figure 5.7, $t\bar{t}$ is the dominant background for events with $E_T^{miss} > 80$ GeV. The number of events after various selection cuts are listed in Table 5.4. Here Cut2, Cut3 and Cut4 are the cuts mentioned in Section 5.2.1 where we defined the event selection criteria of the dilepton

ID	Dataset Name	Generator	Cross Section (pb)	N_{gen}
106400	SU4	Jimmy	47.87	39956
105985	WW	Herwig	11.50	244918
105986	ZZ	Herwig	0.97	229912
105987	WZ	Herwig	3.46	209935
105200	T1	MC@NLO	80.03	707652
108319	DrellYan-mumu	Pythia	1296.2	729929
108320	DrellYan-ee	Pythia	1296.2	779870
108321	DrellYanLowM-mu3	Pythia	2261.4	379963
108322	DrellYanLowM-ee3	Pythia	2240.6	299973

Table 5.1: SU4, diboson, $t\bar{t}$ and Drell-Yan Monte Carlo samples used in this analysis. The dataset name, the generator with which it was produced, the effective cross-section (cross-section×generator-filter-efficiency) are given. In addition, the total number of events generated (N_{gen}) are also listed. Numbers taken from [37].

analysis. In the signal region (i.e. at the level of Cut4 in Table 5.4), the $t\bar{t}$ process gives the maximum background contribution.

ID	Dataset Name	Generator	Cross Section (pb)	N_{gen}
107680	WenuNp0-pt20	AlpgenJimmy	6921.6	2167223
107681	WenuNp1-pt20	AlpgenJimmy	1304.3	601369
107682	WenuNp2-pt20	AlpgenJimmy	378.0	764676
107683	WenuNp3-pt20	AlpgenJimmy	101.9	964659
107684	WenuNp4-pt20	AlpgenJimmy	25.7	229878
107685	WenuNp5-pt20	AlpgenJimmy	7.0	59703
107690	WmunuNp0-pt20	AlpgenJimmy	6919.6	1159826
107691	WmunuNp1-pt20	AlpgenJimmy	1304.2	556882
107692	WmunuNp2-pt20	AlpgenJimmy	378.1	3487974
107693	WmunuNp3-pt20	AlpgenJimmy	102.0	939617
107694	WmunuNp4-pt20	AlpgenJimmy	25.6	229893
107695	WmunuNp5-pt20	AlpgenJimmy	7.0	69958
107700	WtaunuNp0-pt20	AlpgenJimmy	6918.6	1836699
107701	WtaunuNp1-pt20	AlpgenJimmy	1303.2	561843
107702	WtaunuNp2-pt20	AlpgenJimmy	377.8	3488839
107703	WtaunuNp3-pt20	AlpgenJimmy	101.9	874607
107704	WtaunuNp4-pt20	AlpgenJimmy	25.7	234860
107705	WtaunuNp5-pt20	AlpgenJimmy	7.0	58694

Table 5.2: W+jets Monte Carlo samples used in this analysis. The dataset name, the generator with which it was produced, the effective cross-section (cross-section×generator-filter-efficicency) are given. In addition, the total number of events generated (N_{gen}) are also listed. Numbers taken from [37].

ID	Dataset Name	Generator	Cross Section (pb)	N_{gen}
107650	ZeeNp0-pt20	AlpgenJimmy	669.67	2088865
107651	ZeeNp1-pt20	AlpgenJimmy	134.41	1033797
107652	ZeeNp2-pt20	AlpgenJimmy	40.72	384877
107653	ZeeNp3-pt20	AlpgenJimmy	11.30	89953
107654	ZeeNp4-pt20	AlpgenJimmy	2.86	9999
107655	ZeeNp5-pt20	AlpgenJimmy	0.76	4997
107660	ZmumuNp0-pt20	AlpgenJimmy	669.68	5124227
107661	ZmumuNp1-pt20	AlpgenJimmy	134.64	789825
107662	ZmumuNp2-pt20	AlpgenJimmy	40.75	303912
107663	ZmumuNp3-pt20	AlpgenJimmy	11.25	89961
107664	ZmumuNp4-pt20	AlpgenJimmy	2.85	29978
107665	ZmumuNp5-pt20	AlpgenJimmy	0.76	5000
107670	ZtautauNp0-pt20	AlpgenJimmy	669.56	674835
107671	ZtautauNp1-pt20	AlpgenJimmy	134.65	1244685
107672	ZtautauNp2-pt20	AlpgenJimmy	40.76	284907
107673	ZtautauNp3-pt20	AlpgenJimmy	11.27	74960
107674	ZtautauNp4-pt20	AlpgenJimmy	2.84	29982
107675	ZtautauNp5-pt20	AlpgenJimmy	0.76	9993

Table 5.3: Z+jets Monte Carlo samples used in this analysis. The dataset name, the generator with which it was produced, the effective cross-section (cross-section×generator-filter-efficicency) are given. In addition, the total number of events generated (N_{gen}) are also listed. Numbers taken from [37].

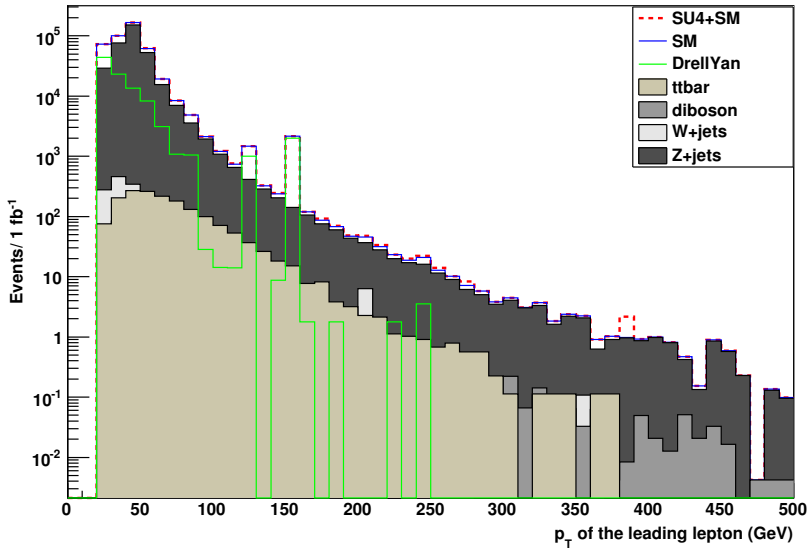

Figure 5.4: Distributions of the p_T of the leading lepton after accepting two opposite sign leptons in fully simulated data.

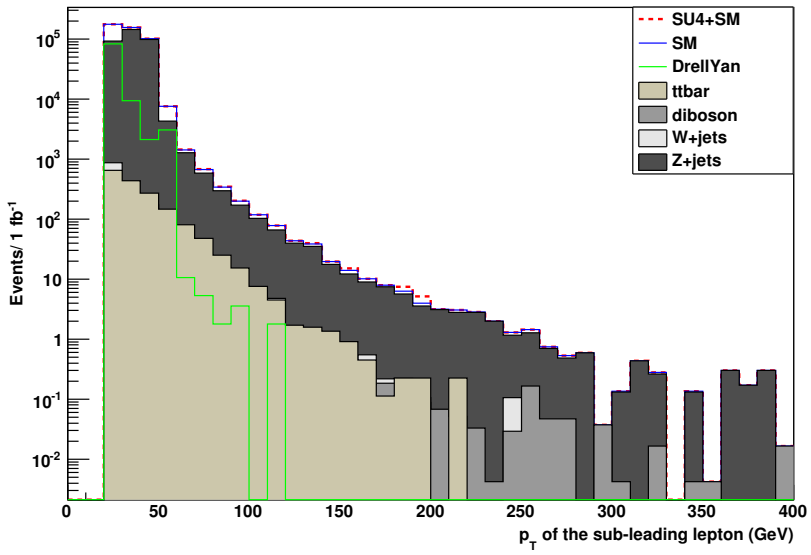

Figure 5.5: Distributions of the p_T of the sub-leading lepton after accepting two opposite sign leptons in fully simulated data.

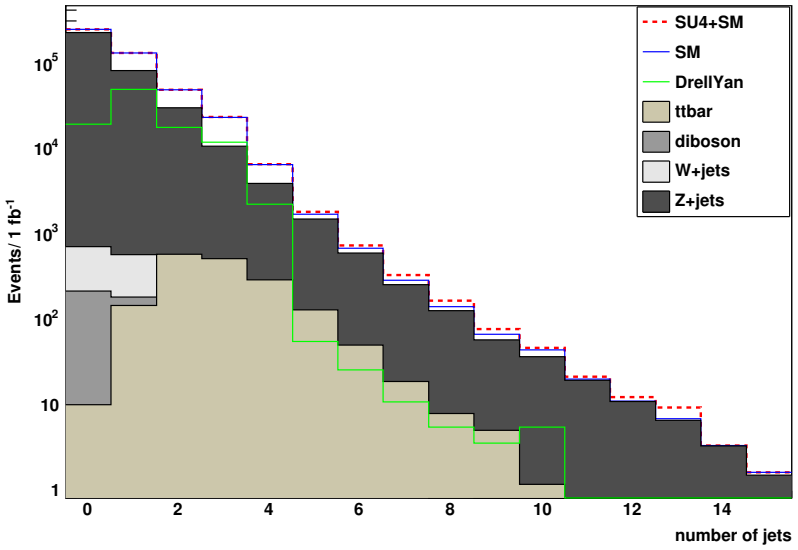

Figure 5.6: Distributions of the total number of jets after accepting two opposite sign leptons in fully simulated data.

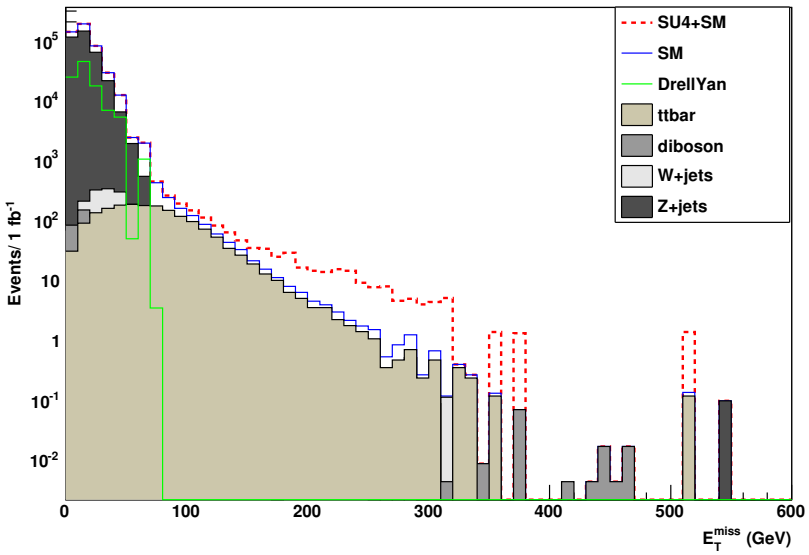

Figure 5.7: Distributions of the missing transverse energy (E_T^{miss}) after accepting two opposite sign leptons in fully simulated data.

Physics Process	2 leptons + 2 jets	Cut2	Cut3	Cut4
SU4	52.0	22.0	9.58	9.58
$t\bar{t}$	559.0	86.0	5.77	4.30
diboson	151.94	4.66	0.06	0.03
Drell Yan	1150.29	11.28	0	0
W+jets	232.54	6.0	0.23	0.12
Z+jets	28965.40	543.85	0.78	0.29
Total SM	31059.17	651.79	6.84	4.74

Table 5.4: Number of events in $1fb^{-1}$ at various event selection levels.

Chapter 6

Data Driven Method for Estimating the $t\bar{t}$ Background

The previous chapter served to provide an overview of the SUSY dilepton analysis. There, we have seen that the most significant background was from $t\bar{t}$ events. The proper understanding of these background processes is essential before one claims a SUSY discovery. For this purpose, data driven methods are usually required to study and estimate the SM backgrounds. In this chapter, our aim is to present a novel data driven technique that we have developed for the estimation of $t\bar{t}$ background. This analysis is based on 7 TeV centre-of-mass energy using fully simulated AODs. Before we focus our discussion on this technique, a general introduction on data driven methods is being provided.

The general aim of data driven methods is to be able to estimate from the data the SM backgrounds and their uncertainties in a signal region, in which new physics may be present [38]. The predictions for SM processes from Monte Carlo models are not perfect because the model is an incomplete representation of the true theory and the simulation of the detector is imperfect. The inaccuracy of these MC models (event generator and detector simulation) contributes systematic uncertainties in the estimation of the SM

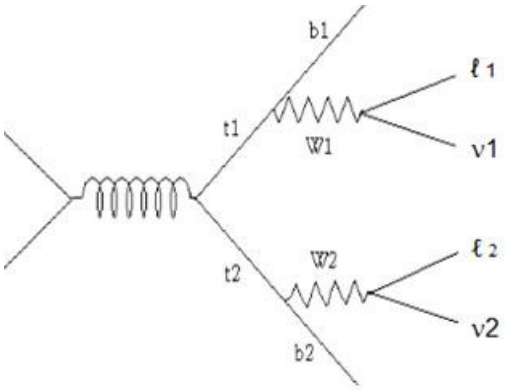

Figure 6.1: Feynman diagram of the $t\bar{t}$ process that contributes to background in the SUSY dilepton search.

backgrounds. Thus, the estimation method cannot rely on MC predictions alone, which is why data driven analysis is strongly desired, i.e., one wants to estimate the background directly from the real data. The background estimation is performed by construction of a control sample, from which predictions in the signal region are derived.

6.1 Construction of $t\bar{t}$ Control Sample

The most significant background for the SUSY dilepton channel is expected to come from $t\bar{t}$ process, where both Ws decay into a lepton and a neutrino, as shown in Figure 6.1. Besides two opposite sign leptons, the SUSY dilepton selection exploits the distributions of kinematic variables related to the two jets, i.e., p_T of the leading and sub-leading jets, missing transverse energy as well as event shape variables, e.g., effective mass.

To constrain the number of $t\bar{t}$ background events using the real data, we need a control sample of events containing jets and leptons having essentially the same kinematic distributions as in the dilepton search channel. One way to achieve this is to select events having four jets and one lepton (4j+1ℓ) as shown in Figure 6.2, rather than two jets and two leptons (2j+2ℓ) shown in Figure 6.1. The only difference between the two Feynman diagrams of $t\bar{t}$ is a W boson decay, i.e., both Ws decay leptonically in Figure 6.1 while

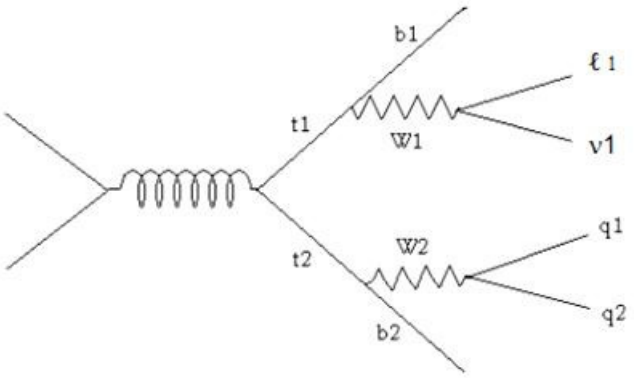

Figure 6.2: Feynman diagram of $t\bar{t}$ process in the control sample.

in Figure 6.2 one of the Ws decays hadronically. This difference populates the final state of $t\bar{t}$ control sample with two additional jets and only one lepton.

As the top quark decays into a bottom quark and a W boson, each $t\bar{t}$ event in the 4j+1ℓ selection should contain two b-jets. We call each of the two tops (i.e. top plus antitop) a *leg* of the event. The leptonic top leg contains a b-jet, a lepton and a neutrino while hadronic top leg is composed of three jets that also includes a b-jet. First, one needs to reconstruct the event, i.e., the hadronic W, the hadronic top, and the leptonic top. Then, excluding the two jets that are from the W, the remaining two jets should have kinematic distributions that are similar to those of two jets in the $t\bar{t}$ background for the 2j+2ℓ search selection. Further, the hadronically decaying W is replaced by a simulated lepton and a neutrino, so that the distributions of the missing energy and event shape variables should be similar to that of the $t\bar{t}$ in the dilepton channel.

The basic steps of the procedure are thus as follows:

1. Select events with four jets and one lepton. Initially this will select not only $t\bar{t}$ but also W+4jets with the W decaying leptonically, but these will be suppressed later by requiring that the event should satisfy $t\bar{t}$ characteristics.

2. Reconstruct the hadronic W, the hadronic top, and the leptonic top using a likelihood-based technique. The likelihood uses both kinematic and flavour tag

information for each particular jet assignment to hadronic and leptonic top legs.

3. In order to reconstruct the leptonic top, one also needs the z-component of the neutrino momentum which one can determine by solving a quadratic equation.

4. From the possible ways of assigning jets for a $t\bar{t}$ event, choose the way with the maximum likelihood. This information is used to estimate the probability of W jet assignment using Bayes theorem. Events are accepted in the control sample only if this probability exceeds a given threshold.

5. The jets identified as those from the W decay are removed and replaced by a simulated lepton-neutrino pair. The choice which jet to replace with a lepton and which with a neutrino is done randomly.

6. The quantities E_T^{miss}, M_{eff} and S_T are recalculated to apply the corresponding requirement as in the 2j+2ℓ selection.

7. Moreover, in the environment of mock and real data, other physics processes are also present besides $t\bar{t}$. These non-$t\bar{t}$ events are suppressed by constructing a statistic that reflects the level of agreement between the event's measured characteristics and the $t\bar{t}$ hypothesis.

For all steps above, we can check using the Monte Carlo truth matching how often the correct assignment of jets is made. For example, one can make a distribution of the mass of the hadronic W candidate for all selected 4j+1ℓ events, and also for that subset of those events where the jets are assigned correctly. We now discuss the above steps in greater detail.

6.1.1 Assignment of jets using Mapping Hypothesis

After accepting events using the 4j+1ℓ selection, next one needs to determine which two jets out of four selected come from a W boson. In order to do so, we use both the

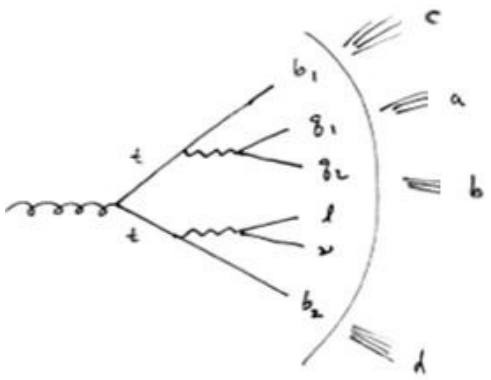

Figure 6.3: Illustration of the hypothesis tested with the 4j+1ℓ control sample.

kinematic and flavour tag information. Of the four jets in each event selected for the control sample, two of these should be b jets, and the other two should come from the hadronic decay of the W (here called W jets). Of course in some of the selected events this may not be the case. For example, one of the b jets may have gone missing, and an additional gluon jet was reconstructed. It means, when one of the b jets fails to survive cuts in 4j+1ℓ selection, and instead a gluon jet may pass the cuts and accepted as a fourth jet. These possibilities are further discussed in Section 6.2. Nevertheless if we make the hypothesis that in the control sample two of the jets are b jets, and the other two are from a W decay, and we then can find the jet assignment that maximises the likelihood of this hypothesis.

A jet assignment hypothesis is illustrated in Figure 6.3. The b jet that accompanies the hadronically decaying W is denoted b_1, the up-type quark jet (i.e., u or c) from the W decay is called q_1, the down-type jet (d, s or b) is called q_2, and the b jet that accompanies the leptonically decaying W is called b_2.

Each selected event has four reconstructed jets, labelled by indices a, b, c, d. Each jet is characterized by a flavour tag weight w, related to the presence or absence of tracks that do not extrapolate back to the primary vertex. In addition we have the four-momenta of the reconstructed jets, that of the lepton, and the missing transverse

energy E_T^{miss}. From this we can estimate the momentum vector of the missing neutrino up to a two-fold ambiguity.

A particular assignment of the reconstructed jets onto the hypothesis described above would be, e.g., $b_1 = c$, $q_1 = a$, $q_2 = b$, $b_2 = d$ as illustrated in Figure 6.3. There are 24 possible assignments, so we will compute 24 likelihood values. For the likelihood we can write $L(q_1, q_2, b_1, b_2)$, i.e., the arguments represent, in the given order, the indices of the reconstructed jets assigned to q_1, q_2, b_1 and b_2. For a choice of the reconstructed jets a b, c, d, we can model the likelihood as

$$\begin{aligned} L(a,b,c,d) &= \frac{1}{\sqrt{2\pi}\sigma_{W_\mathrm{h}}} e^{-(m_{ab}-M_W)^2/2\sigma^2_{W_\mathrm{h}}} \; \frac{1}{\sqrt{2\pi}\sigma_{t_\mathrm{h}}} e^{-(m_{abc}-m_t)^2/2\sigma^2_{t_\mathrm{h}}} \\ &\times \frac{1}{\sqrt{2\pi}\sigma_{W_\mathrm{l}}} e^{-(m_{dl\nu}-m_t)^2/2\sigma^2_{t_\mathrm{l}}} \\ &\times L_W(w_a, w_b)\; L_{bb}(w_c, w_d)\;. \end{aligned} \tag{6.1}$$

Here the first three Gaussian terms use the information on the invariant mass of different jet combinations. We want jets a and b to have an invariant mass close to the mass of W boson M_W, and the mass of jets a, b and c should be close to the mass of top quark m_t. Also, the invariant mass of jet d with the lepton and neutrino should have a mass close to m_t, where for this one needs to use an estimate for the z component of the neutrino's momentum. For this we assume that some strategy has been used to resolve the two-fold ambiguity, which is discussed in Section 6.1.2. The values of σ_{W_h}, σ_{t_h} and σ_{t_l} can be estimated from Monte Carlo studies that exploit truth information.

The final two terms in Equation (6.1) represent the likelihood for the four measured values of the flavour tag weight. The first two values, w_a and w_b, are hypothesised to come from the up-type and down-type quark jets, respectively, of the hadronic W decay, and the latter two values, w_c and w_d, are hypothesized to be from b-jets. For the two

jets from the W decay, we can write the likelihood as

$$L_W(w_a, w_b) = \sum_{i,j} P_{ij} f(w_a|i) f(w_b|j) \ , \tag{6.2}$$

where the index i is summed over the flavours u and c, and j is summed over d, s and b. The coefficients P_{ij} represent the probability of the flavour combination ij for the W decay. If we neglect the phase-space suppression for W decays to different quark flavours (except for top, which is completely suppressed), then the probabilities P_{ij} can be written

$$P_{ij} = \frac{|V_{ij}|^2}{\sum_{i,j} |V_{ij}|^2} \ , \tag{6.3}$$

where V_{ij} is the relevant CKM matrix element and where in the denominator the indices i and j are summed over the kinematically accessible quark flavours for up and down-types, respectively ($i = u, c$, $j = d, s, b$). In this way, the part of the likelihood function that describes the vertex properties of the jets from the W takes into account the correlations between the flavours of the up- and down-type jets. (This would be even more powerful if one had a measure that distinguished u and d jets from s jets.)

For the functions $f(w|u)$, $f(w|d)$ and $f(w|s)$, it should be sufficient to use an averaged distribution of w predicted for "light" jets, i.e., u, d, or s. We denote this as $f(w|l)$ (with l standing for "light"). The functions $f(w|c)$ and $f(w|b)$ give the distributions for c and b jets, both of which contain in general displaced vertices.

The final term in Equation (6.1) represents the likelihood of the b-jet hypothesis for the two final b-tag weights. It can be written

$$L_{bb}(w_c, w_d) = f(w_c|b) f(w_d|b) \ . \tag{6.4}$$

The pdfs $f(w|i)$ for $i = l, c, b$ can be obtained from Monte Carlo histograms, parame-

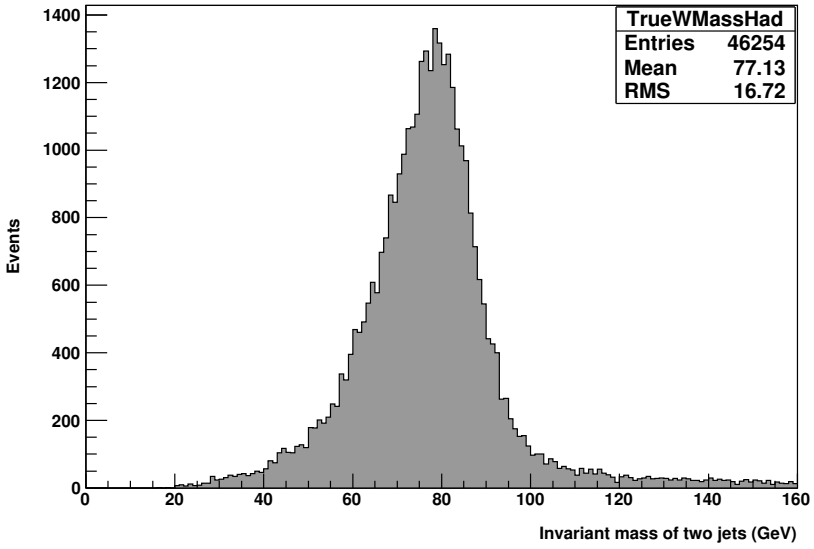

Figure 6.4: Invariant mass distribution of two jets that are coming from the hadronic W boson decay.

terised with a smooth function.

6.1.2 Determination of Kinematic Terms

In order to calculate the kinematic terms of the likelihood in Equation 6.1, i.e., the first three Gaussian terms, one also needs to know the values of σ_{W_h}, σ_{t_h} and σ_{t_l}. One can estimate these values with the help of the invariant mass distributions of jets. For example, σ_{W_h} can be determined by plotting invariant mass distribution of two jets that belong to the hadronic W decay. The identification of these jets is made by investigating Monte Carlo truth information. The RMS value shown in Figure 6.4 is a good estimate for σ_{W_h}, i.e., 16.72. Similar procedure is adopted to estimate the values of σ_{t_h} and σ_{t_l}, which are found to be 26.4 and 43.4 respectively.

Another kinematic term that needs to be determined is the z component of the neutrino momentum that belongs to the leptonic top leg. The system of equations describing the kinematics of the leptonic decay of W can be expressed by

$$E_{\nu}^2 = p_{\nu_x}^2 + p_{\nu_y}^2 + p_{\nu_z}^2 \tag{6.5}$$

$$m_W^2 = (E_\ell + E_\nu)^2 - (p_{\ell_x} + p_{\nu_x})^2 - (p_{\ell_y} + p_{\nu_y})^2 - (p_{\ell_z} + p_{\nu_z})^2 \tag{6.6}$$

$$E_{T_x}^{miss} = p_{\nu_x} \tag{6.7}$$

$$E_{T_y}^{miss} = p_{\nu_y} \tag{6.8}$$

where E_ν and E_ℓ are the energies of the neutrino and lepton respectively, and (p_{ν_x}, p_{ν_y}, p_{ν_z}) and (p_{ℓ_x}, p_{ℓ_y}, p_{ℓ_z}) are the x, y and z components of momenta of neutrino and lepton respectively. The right-hand side of Equation 6.6 gives the invariant mass squared of the lepton-neutrino pair, and this is set equal to m_W^2, the mass squared of the W boson. $E_{T_x}^{miss}$ and $E_{T_y}^{miss}$ relate the projection of E_T^{miss} onto the transverse axes x and y respectively.

The above system of equations can be reduced to a quadratic equation in p_{ν_z} which one can solve to determine the z component of neutrino momentum up to a two-fold ambiguity. The strategy usually used inside the ATLAS collaboration is to take the smaller of the two p_z values because leptons (charged and the neutrino) are expected to have high transverse momentum p_T and they do not have much momentum along the z-axis (beam axis), so the solution with the smallest p_z is more likely to be the right one [39]. Therefore, we have also chosen the smaller of the two p_z values for this analysis. Moreover, when the quadratic equation has no solution, we throw away the event.

6.1.3 Parameterisation of Flavour Tag Distribution

In order to compute the likelihood in Equation 6.1, one also needs to determine the flavour tag weight terms. The flavour tag weight w is a discriminating variable used to separate b-, c- and light-jets. As each $t\bar{t}$ decay produces two b quark jets (or b-jets),

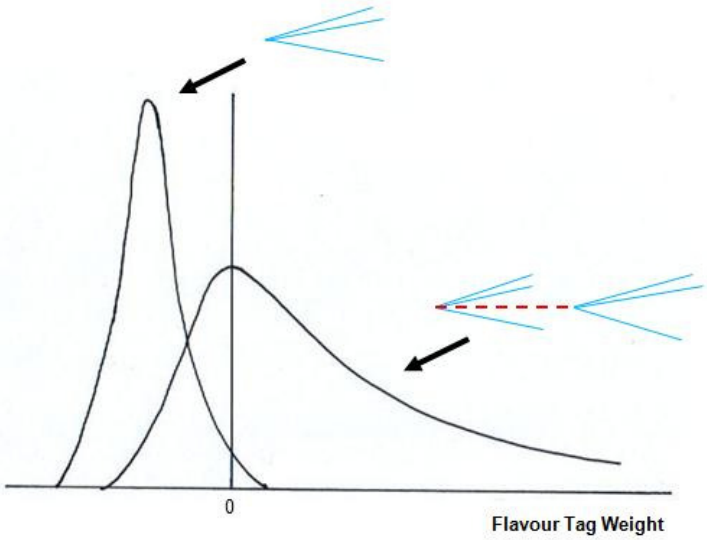

Figure 6.5: Cartoon representing two flavour tag distributions.

the identification of these b-jets helps to determine which two jets correspond to the hadronic decay of the W. The b-jets possess several characteristic properties that can be utilised to separate them from jets coming from the hadronisation of lighter quarks (light-jets). The most important property is the relatively long lifetime of b-hadrons of about 1.5 ps [5]. This leads to a measurable flight length of a few millimetres before their subsequent decay, i.e., the decay of b-hadron produces a displaced decay vertex or secondary vertex. In short, the value of the flavour tag weight w reflects presence or absence of a secondary vertex. A cartoon representing two distributions of flavour tag weight is shown in Figure 6.5. One can see that the distribution on the left does not contain secondary vertex therefore, it has lower values of flavour tag weights w. The tag weight distribution of light-jets is very similar to the shape of this distribution. The other distribution in Figure 6.5 which is skewed towards the higher tag weight values correspond to those jets in which the secondary vertex is present e.g. b-jet.

There are various flavour tagging methods studied in ATLAS. One such method is *spatial taggers* that utilise lifetime information like secondary vertices and impact parameters. The spatial tagger that has been used in this thesis is IP3D+SV1 tagger.

The tagging technique and performance of IP3D+SV1 tagger is detailed in [19].

To compute the likelihood terms in Equation 6.2 and Equation 6.4, one requires probability density functions (pdfs) $f(w|i)$ for i = b-, c- and light-jets. These pdfs can be obtained from Monte Carlo histograms parameterised with smooth functions. We have parameterised the tag weight distribution with Johnson distribution which is defined as [40]

$$\begin{aligned} f(w) &= \frac{\eta}{\sqrt{2\pi}} \frac{1}{\sqrt{(w-\epsilon)^2+\lambda^2}} \\ &\times \exp\left(-\frac{1}{2}\left(\gamma + \eta \ln\{\frac{w-\epsilon}{\lambda} + \sqrt{\frac{(w-\epsilon)^2}{\lambda^2}+1}\}\right)^2\right) \end{aligned} \tag{6.9}$$

where η and γ are shape parameters, λ is scale parameter, ϵ is location parameter and w is the tag weight. The parameters η, ϵ, γ and λ are estimated by minimising the quantity

$$\chi^2 = 2\sum_{i=1}^{N}(n_i \log\frac{n_i}{\hat{\nu_i}} + \hat{\nu_i} - n_i) \tag{6.10}$$

using the MINUIT package [41]. The Equation 6.10 is taken from the Ref [42]. Here N is the total number of bins in the histogram and n_i is the content of bin i. Each bin is assumed to be Poisson distributed, i.e., $n_i \sim \text{Poisson}(\nu_i)$ and ν_i is the mean value of bin i and $\hat{\nu_i}$ is the estimator of ν_i. The MC histogram of the light-jet along with the fitted function in blue and red colours respectively are shown in Figure 6.6. c- and b-jets distributions along with their fitted functions are shown in Figure 6.7 and Figure 6.8 respectively.

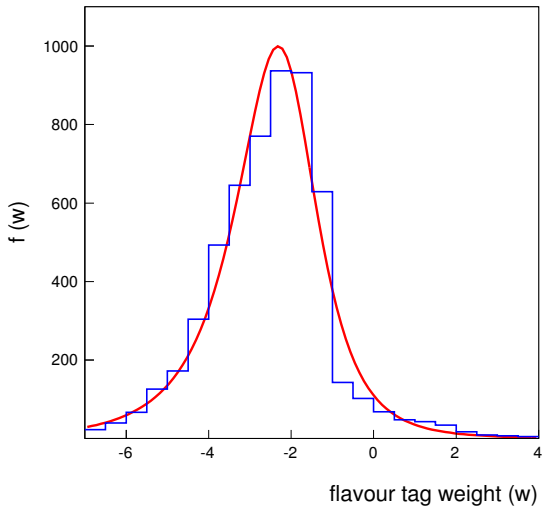

Figure 6.6: Tag weight distribution of light-jets along with the fitted function.

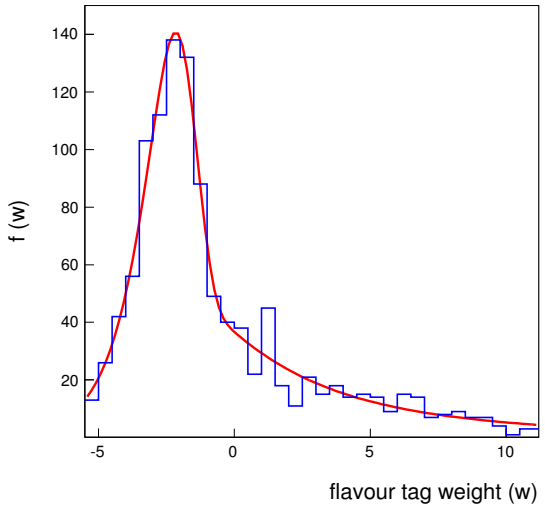

Figure 6.7: Tag weight distribution of c-jets along with the fitted function.

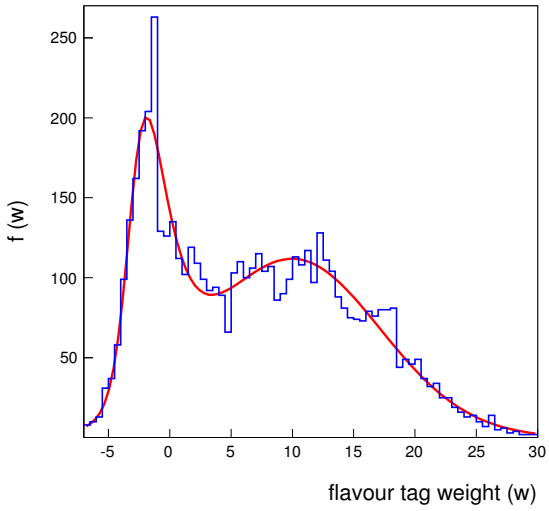

Figure 6.8: Tag weight distribution of b-jets along with the fitted function.

6.1.4 Identification of Jets using Probability of W Jet Assignment

Once the unknowns in the kinematic and flavour tag terms are determined, one can compute the likelihood in Equation 6.1. As 24 jet assignments are possible, one needs to calculate 24 likelihood values corresponding to each jet assignment. Of the 24 hypotheses H_k, $k = 1, ..., 24$, the one which gives the maximum likelihood is denoted $\hat{H}$. We can then estimate the probability P_{CA} that $\hat{H}$ assigns correctly the two jets from the W. A probability of any hypothesis (H_k) for mapping of reconstructed jets onto q_1, q_2, b_1 and b_2 can be obtained from Bayes' theorem as

$$P\left(H_k|\,\vec{m},\vec{w}\right) = \frac{L\left(\vec{m},\vec{w}\,|H_k\right)\pi(H_k)}{\sum_{i=1}^{24} L\left(\vec{m},\vec{w}\,|H_i\right)\pi(H_i)} \tag{6.11}$$

where $\vec{m} = (m_{ab}, m_{abc}, m_{dl\nu})$ is the set of measured invariant masses and $\vec{w}$ is the set of flavour tag weights defined in Equation 6.1. $L\left(\vec{m},\vec{w}\,|H_k\right)$ is the likelihood, k is an integer which can take any value between $1 \leq k \leq 24$. $\pi(H_k)$ and $\pi(H_i)$ are the prior probabilities which can be taken as $1/24$.

It is clear from Figure 6.3 that out of 24 possible jet assignments, 4 represent correct assignments of the two jets from the W decay. That is, if $\hat{H}$ assigns the two W jets correctly, then swapping q_1 and q_2 would still be correct, as would be obtained as well from swapping b_1 and b_2, or both q_1, q_2 and b_1, b_2. These have probabilities $P(\hat{H}|\,\vec{m}, \vec{w})$, $P(\hat{H}, q_1 \leftrightarrow q_2 \mid \vec{m}, \vec{w})$, $P(\hat{H}, b_1 \leftrightarrow b_2 \mid \vec{m}, \vec{w})$ and $P(\hat{H}, q_1 \leftrightarrow q_2, b_1 \leftrightarrow b_2 \mid \vec{m}, \vec{w})$. $\hat{H}_{q_1 \leftrightarrow q_2}$ is the hypothesis when q_1 and q_2 of $\hat{H}$ are swapped. $\hat{H}_{b_1 \leftrightarrow b_2}$ is the hypothesis when b_1 and b_2 of $\hat{H}$ are swapped. Finally, $\hat{H}_{q_1 \leftrightarrow q_2,\ b_1 \leftrightarrow b_2}$ is the hypothesis when both q_1, q_2 and b_1, b_2 of $\hat{H}$ are swapped. Thus, the probability of correct W jet assignment (P_{CA}) is

$$P_{CA} = \frac{L(\vec{m}, \vec{w} \mid \hat{H}) + L(\vec{m}, \vec{w} \mid \hat{H}_{q_1 \leftrightarrow q_2}) + L(\vec{m}, \vec{w} \mid \hat{H}_{b_1 \leftrightarrow b_2}) + L(\vec{m}, \vec{w} \mid \hat{H}_{q_1 \leftrightarrow q_2,\ b_1 \leftrightarrow b_2})}{\sum_{i=1}^{24} L\left(\vec{m}, \vec{w} \mid H_i\right)} \tag{6.12}$$

What is important here is that P_{CA} is a number that can be obtained for real data. No Monte Carlo truth information is required, beyond what was used to determine the form of the likelihood function. Therefore, we can cut on P_{CA} to select events where the assignment of the W jets should be reliable. The distribution of P_{CA} normalized to $1fb^{-1}$ of integrated luminosity is shown in Figure 6.9. The higher values of P_{CA} corresponds to the higher probability of identifying correctly the jets from the W. We require $P_{\mathrm{CA}} \geq P_{\mathrm{CA,min}}$ in order to ensure that the events in the control sample have their W jets correctly identified with reasonably high probability. The value of $P_{\mathrm{CA,min}}$ will be determined on the basis of studies discussed in Section 6.3.

6.1.5 Determination of Scale Factor

It was discussed earlier that once the jets from the W are identified, one needs to replace them with simulated lepton and neutrino. After this replacement, the number of leptons and jets in both $4j + 1\ell$ and $2j + 2\ell$ selections become equal. Then, one can apply the similar search selection cuts to the control sample. But, the total rates for $t\bar{t}$

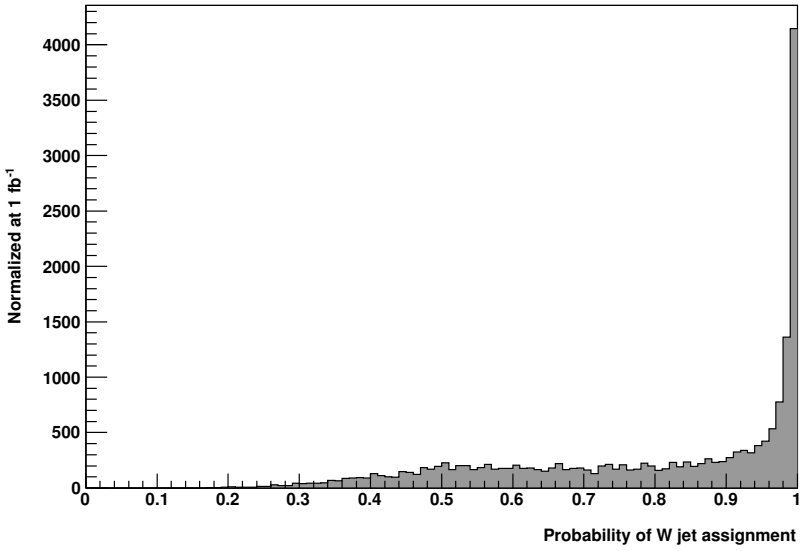

Figure 6.9: The probability distribution of correct jet assignment normalized to $1\,\mathrm{fb}^{-1}$ of integrated luminosity.

events using $2j + 2\ell$ and $4j + 1\ell$ selections will differ because of the different branching ratios (BR) for the leptonic and hadronic W decay, i.e., $BR(W \to \mu \text{ or } e) \cong \frac{2}{9}$ and $BR(W \to \text{hadrons}) \cong \frac{2}{3}$, and because of the limited efficiency with which one identifies the two jets that come from the W decay. After defining a final set of cuts for SUSY search and a corresponding set of final cuts for the control sample, the ratio of rates, called scale factor, is given by

$$\tau = \frac{t\bar{t} \text{ events survived in the control sample}}{t\bar{t} \text{ events survived in the dilepton search sample}} , \tag{6.13}$$

where both numerator and denominator correspond to the same effective luminosity L_{MC}, which should be as high as possible to obtain the most accurate determination of the scale factor τ. The point of carrying out the analysis in this way is that the systematic uncertainty in our estimate of τ is expected to be much smaller than the uncertainty in an estimate of $t\bar{t}$ background based solely on Monte Carlo. This is because τ is formed using

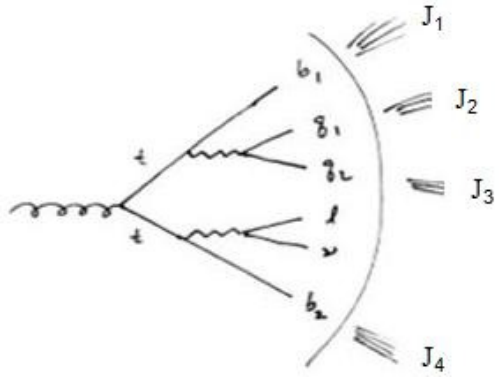

Figure 6.10: Schematic diagram of parton-jet matching used for the identification of jets.

a ratio in which most of the systematic errors are expected to cancel. The uncertainty in the determination of top background was estimated to be 20% corresponding to an integrated luminosity of $1\,\mathrm{fb}^{-1}$ [19].

6.2 Identification of Jets using Parton Jet Matching

In the previous section, the 4 jets of the control sample were identified by choosing the jet assignment with the highest likelihood and further requiring $P_{\mathrm{CA}} \geq P_{\mathrm{CA,min}}$. In this section, our aim is to use the Monte Carlo truth information to determine what fraction of the time this assignment is actually correct. This step is needed for optimising the jet identification technique used in the previous section. A schematic diagram of parton-jet matching used in this analysis is shown in Figure 6.10.

Here q_1 and q_2 are the partons (or quarks) coming from hadronic W decay, and b_1 and b_2 are two b quarks produced in $t\bar{t}$ decay. J_1, J_2, J_3 and J_4 are the 4 reconstructed jets selected in the $t\bar{t}$ control sample. If these reconstructed jets are initiated by the partons shown in Figure 6.10, they should be roughly in the same direction as that of their corresponding partons. For example in Figure 6.10, the direction of J_1 and b_1 looks very similar, and therefore one can say b_1 and J_1 are a matched pair of parton and jet. In order to match a parton and a jet direction quantitatively, we compute a quadratic

sum of $\triangle R_{ij}$ as

$$\triangle R_k = \sqrt{\sum_{i,j} (\triangle R_{ij})^2} \tag{6.14}$$

where $i = (b_1, q_1, q_2, b_2)$ and $j = (J_1, J_2, J_3, J_4)$ represent partons and jets respectively as shown in Figure 6.10. $\triangle R$ is the usual geometrical variable defined as $\triangle R = \sqrt{(\triangle\eta)^2 + (\triangle\phi)^2}$. Here, the difference ($\triangle$) is between a parton and a jet, i.e., between i and j. There are 24 possible arrangements among the partons and the jets, but only one particular case is shown in Figure 6.10, i.e., J_1 corresponds to b_1, J_2 corresponds to q_1, J_3 corresponds to q_2 and J_4 corresponds to b_2. $\triangle R_k$ is the overall $\triangle R$ where subscript k, which labels the assignment of partons to jets, is an integer between $1 \leq k \leq 24$. Each $\triangle R_k$ value represents a particular parton-jet arrangement. Then, we select the minimum of 24 $\triangle R_k$ values, which we call $\triangle R_{\mathrm{Min}}$. The minimum of $\triangle R_k$ value is computed for every event and is shown in Figure 6.11.

Further, in each minimum value of overall $\triangle R$ we also find the individual term $\triangle R_{ij}$ that gives the maximum contribution in the quadratic sum of $\triangle R_{ij}$ (Equation 6.14). A plot of the maximum individual term of the overall $\triangle R$ minimum called δR_{Max} is shown in Figure 6.12. The spike below 0.5 in Figure 6.12 represents those events when all four partons are matched with the four reconstructed jets. The values above 1.0 corresponds to the cases when not all four jets are matched but some of them may be well matched. This happens because cuts (i.e. $|\eta| < 2.5$ and $p_T^{jet} > 20$ GeV) are being applied to the reconstructed jets before accepting them in the control sample. Therefore, if any jet originated from the partons, shown in Figure 6.10, fails to survive these cuts will be lost, and instead some other jet may pass the cuts and accepted as a fourth jet in the control sample. It means, if the fourth accepted jet is not originated from the above partons then its direction is expected to be different than the directions of the reconstructed jets (J_1, J_2, J_3, J_4) shown in Figure 6.10. Consequently, the fourth accepted jet will not find a

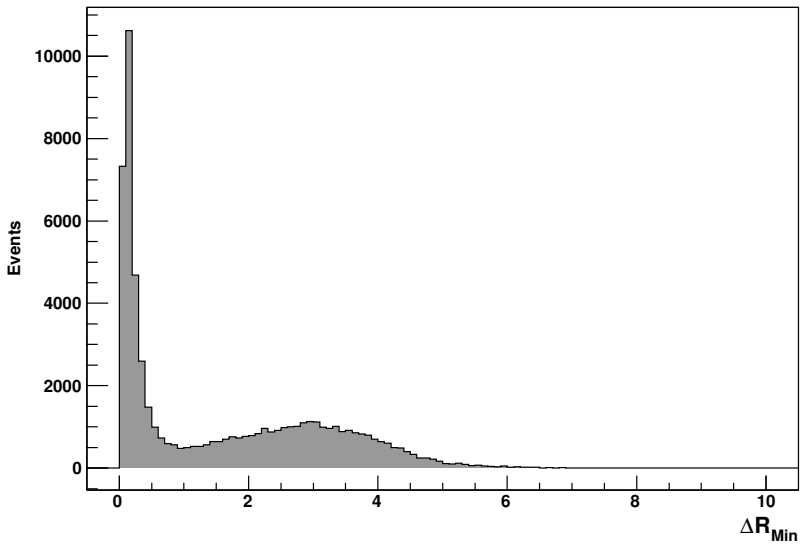

Figure 6.11: Distribution of the minimum value of overall $\triangle R$.

well matched parton. Moreover, if the lost jet is one of the b jets and the fourth accepted jet is a light jet, then it will also affect the jet identification characteristics defined in the likelihood (Equation 6.1). Because the flavour tag weight of a light jet is usually significantly lower than a b jet while our likelihood based technique identifies b jets with the help of high tag weights. To ensure all the partons (b_1, q_1, q_2, b_2) in Figure 6.10 are well matched with the reconstructed jets (J_1, J_2, J_3, J_4), a cut value on δR_{Max} is needed. For purposes of the optimisation studies done in this section, a cut value of 1.0 has been used, i.e., all parton-jet pairs are considered to be well matched when $\delta R_{\mathrm{Max}} < 1.0$.

6.3 Frequency of Correctly Identified Jets

We now summarise our strategy for $t\bar{t}$ background estimation:

1. Select $4j + 1\ell$ events that are compatible with $t\bar{t}$.

2. Identify 2 jets that correspond to the W and replace them with an $\ell\nu$ pair.

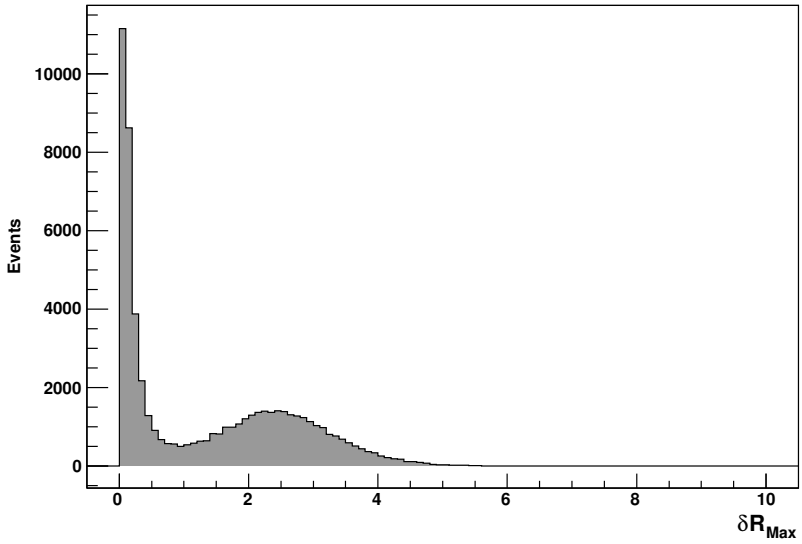

Figure 6.12: Distribution of the maximum individual term of the overall $\triangle R$ minimum.

3. Apply cuts to the control sample identical to those used in the dilepton search sample.

4. Estimate $t\bar{t}$ background rate in the search sample using the control sample.

As described in Section 6.1, the 2 jets (point 2 above) are identified using the likelihood of each jet assignment and by requiring the estimated probability to have found the W jets exceeds a given threshold (Equation 6.12). We expect that the 2 W jets are not always correct but a mixture of correct and incorrect fractions. To study how often we get the correct jet pairs, the 2 Wjets are matched with the Monte Carlo truth. In this connection, three distributions of probability of correct jet assignment that correspond to three different cases are shown in Figure 6.13. It can be seen from Figure 6.13 that if the 2 Wjets are accepted in the $4j + 1\ell$ events, then the frequency of their correct identification is high. The frequency of the correct identification of 2 W jets is dependent on the threshold value of P_{CA}. That is if the threshold is set at the lower values (say 0.3), then the chances for the correct identification of 2 W jets is low, even though the

event acceptance rate in the control sample is high. On the other hand, if the threshold $P_{\mathrm{CA,min}}$ is high (say 0.95), then the 2 W jets are correctly identified with high frequency. In this case, the event statistics of the $t\bar{t}$ will be small. As mentioned in the point 2 above, the identified 2 W jets are then replaced with an $\ell\nu$ pair, therefore these jets should be correctly identified so that the later part of the analysis gives better results. Thus, a cut value of 0.9 is chosen for this analysis, i.e. $P_{\mathrm{CA,min}} = 0.9$, which is also shown in Figure 6.13. Quantitatively, out of $4j + 1\ell$ accepted events, 51% of the time the 2 Wjets are correctly identified. The invariant mass distribution of two identified W jets is shown in Figure 6.14. In this figure, the invariant mass distribution of correctly identified 2 W jets is also shown. The correct jet fraction is not very high because only 59% of the cases the 4 selected jets actually contain 2 Wjets. When the 2 Wjets are present in the $4j + 1\ell$ events, then 87% of the time we found the correct W jets. Moreover, if 4 selected jets contain 2 Wjets and 2 $b$jets, then 2 identified Wjets are 91% correct.

The above results suggest for the modification in the event selection procedure, not yet carried out in this analysis, so that the acceptance fraction of 2 Wjets is significantly higher than 59%. One way to achieve this is to relax the selection cuts on pseudorapidity $|\eta|$ and transverse momentum p_T of jets, and to accept four or more jets in the control sample instead of requiring exactly four jets ($4j + 1\ell$ selection). The proposed solution is not easily manageable. For example, in the $4j + 1\ell$ selection, 24 jets assignments are possible which is not very complex when we do the calculation for the likelihood. But, when the number of jets in the control sample are 5 ($5j + 1\ell$ selection) and 6 ($6j + 1\ell$ selection), then 120 and 720 likelihood calculations will be needed respectively. It means that the task of finding $\hat{H}$ becomes very laborious. Further, in the $4j + 1\ell$ selection, the presence of the two b jets makes the task of finding the two W jets much simpler. That is, the two b jets are isolated because of the presence of the secondary vertex, i.e. the high flavour tag weight w values, and what remains are the two W jets. But after the

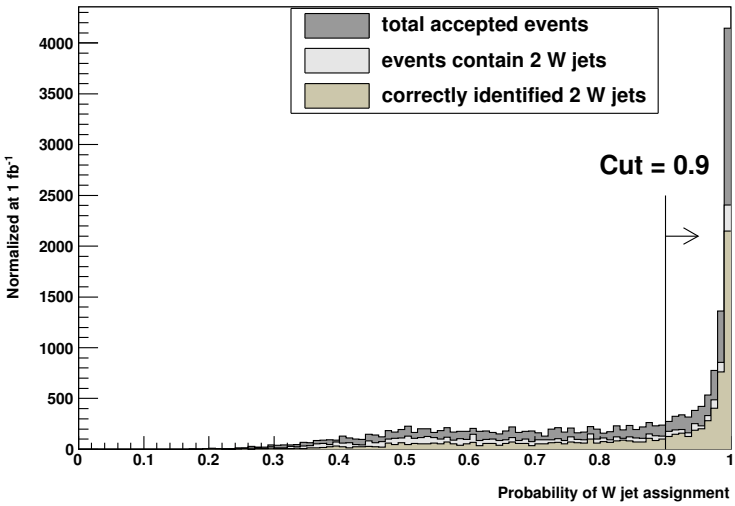

Figure 6.13: The probability distribution of correct jet assignment for three different cases normalized to $1\,\mathrm{fb}^{-1}$ of integrated luminosity.

identification of the two b jets in the $5j + 1\ell$ and $6j + 1\ell$ selections, it will be difficult to find which 2 of 3 and 2 of 4 remaining jets respectively correspond to the 2 W jets. Also, when 2 W jets are identified, then one needs to apply the selection cuts similar to those used in the dilepton search sample. That is, the remaining part of the 5 and 6 jets analyses will be similar to the $4j + 1\ell$ selection.

6.4 Comparison of Distribution Shapes

In order to test how well the $t\bar{t}$ control sample is, one needs to compare the distributions from $t\bar{t}$ in the $2j + 2\ell$ selection (dilepton search sample) to those from $t\bar{t}$ in the $4j + 1\ell$ selection (control sample). These distributions should have a very similar shape. All distributions are normalized to unit area so that their shapes can be compared. In all the plots shown below, the blue line denotes the variable distribution in the dilepton search sample while the red line corresponds to the same variable distribution in the control sample.

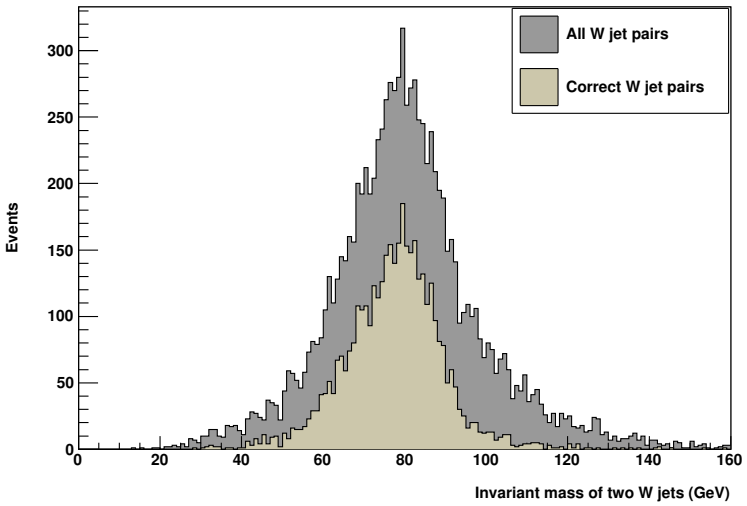

Figure 6.14: Invariant mass distributions of all W jet pairs and correctly identified W jet pairs.

First, we will compare the distribution shapes of two jets that do not come from the hadronic W decay. In the earlier sections, the two jets which correspond to the W have been identified first by using flavour tag weight and kinematic information and then using parton and jet matching. The two identified jets are then replaced with simulated lepton and neutrino, and what remains are those jets that do not belong to the W. The distributions of the transverse momenta of the leading and sub-leading jets are compared in Figures 6.15 and 6.16 respectively. Here, Monte Carlo truth information is used to identify jets. It is clear from these plots that the two jet system from $4j + 1\ell$ selection is very similar to that of $2j + 2\ell$ selection. As one does not have access to partons in real data therefore, when the matching is based on measurable quantities such as flavour tag weights, then such a good agreement is not necessarily expected.

Now we will compare the jet distributions in those cases when the matching is based on measurable quantities instead of MC truth. The distribution of the transverse momentum (p_T) of the leading jet is shown in Figure 6.17. One can see that the level of agreement is not as good as in Figure 6.15 when the matching was based on MC truth.

Similar result is obtained for the distribution of the p_T of the sub-leading jet as shown in Figures 6.19 and 6.16.

The discrepancy in the results occur because the distributions depend on whether or not the two identified W jets, that are replaced with simulated lepton and neutrino, really came from the W. It means if the 2 W jets are correctly identified, then the distributions are in better agreement. Therefore, the distributions have also been compared in those cases when the W jets are correctly identified as shown in Figure 6.18 and 6.20.

Next we will compare the distribution shapes of the missing transverse energy E_T^{miss}. In the $2j + 2\ell$ selection, the final state contains two neutrinos which are the source of missing energy in the $t\bar{t}$ dilepton event. On the other hand, the $4j + 1\ell$ selection has only one neutrino and therefore we need to replace two jets with simulated lepton and neutrino to make the kinematics similar. Therefore, it is required to recalculate the missing transverse energy by including the information of a simulated neutrino. After this modification, we can compare the distributions, which are shown in Figure 6.21. It can be seen in Figures 6.21 and 6.22 that the distribution shape of missing transverse energy is not strongly dependent on the correct identification of W jets as we saw in case of the distributions of the jets. Finally, the distribution shapes of the effective mass M_{eff} are compared in Figure 6.23. Like jets, M_{eff} is also strongly dependent on the correct identification of 2 W jets as can be seen in Figure 6.24.

It is clear from the above plots that the distributions of kinematic and event shape variables in the control sample are not in perfect agreement to those of the dilepton search sample. The main reason for these disagreements is the low frequency of finding the correct W jets, i.e. 51%. It has been discussed earlier that out of $4j + 1\ell$ selected events, only 59% of the time the 4 accepted jets actually contain 2 W jets thats why the frequency of correct W jets is low. Moreover, the differences in the above distributions introduce systematic uncertainty in the estimate of scale factor τ, and its treatment has been discussed in Sections 7.4.

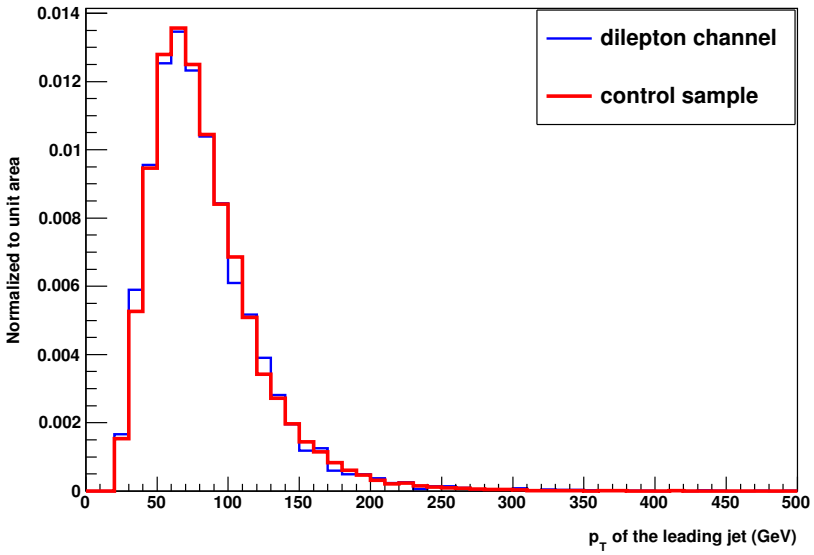

Figure 6.15: Distribution of p_T of the leading jet for simulated $t\bar{t}$ events passing the dilepton selection and for the control sample. The identification of jets in the control sample is based on the MC truth information.

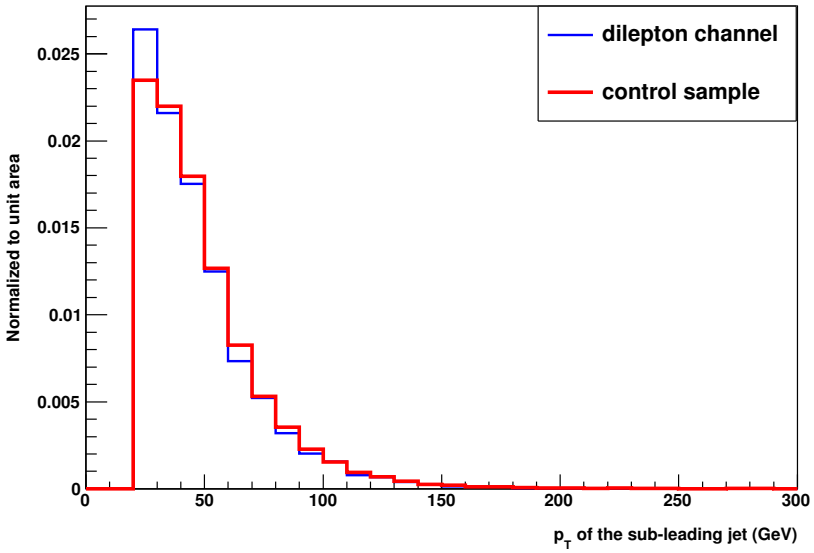

Figure 6.16: Distribution of p_T of the sub-leading jet for simulated $t\bar{t}$ events passing the dilepton selection and for the control sample. The identification of jets in the control sample is based on the MC truth information.

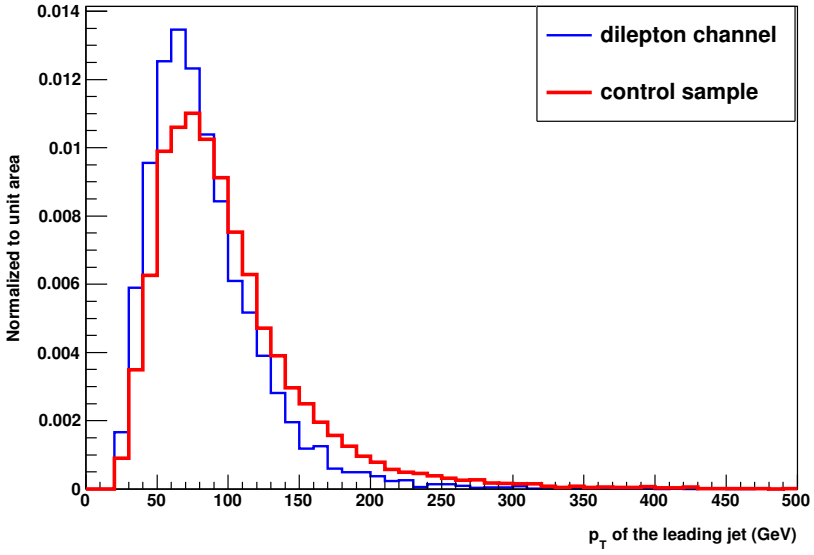

Figure 6.17: Distribution of p_T of the leading jet for simulated $t\bar{t}$ events passing the dilepton selection and for the control sample. The identification of jets in the control sample is based on the measurable quantities.

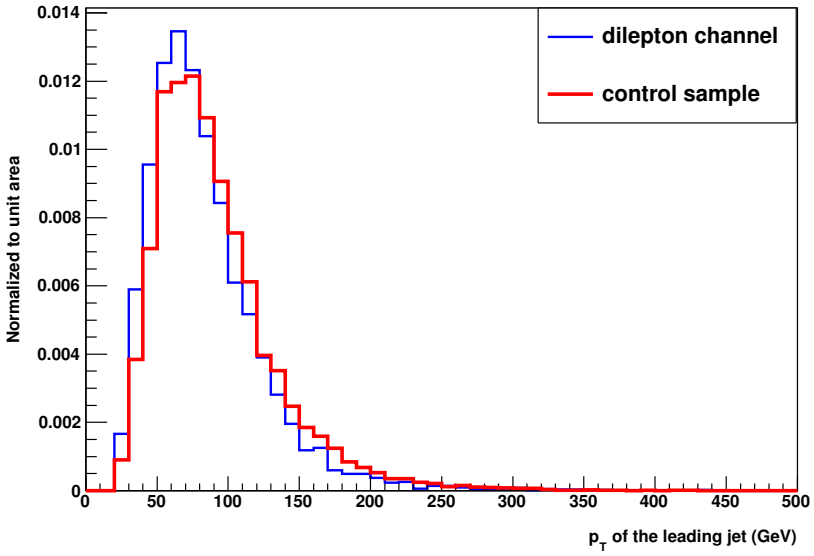

Figure 6.18: Distribution of p_T of the leading jet for simulated $t\bar{t}$ events passing the dilepton selection and for the control sample. The identification of jets in the control sample is based on the measurable quantities. Only those events are compared which contain correct W jets.

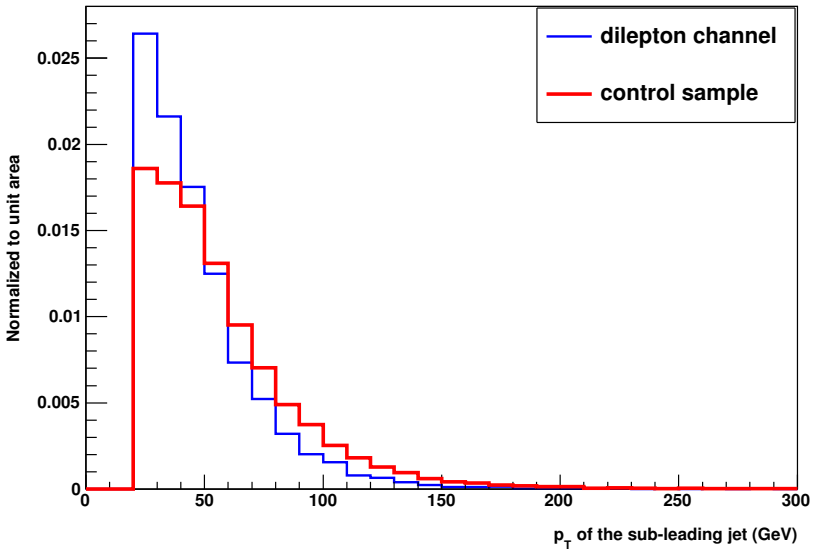

Figure 6.19: Distribution of p_T of the sub-leading jet for simulated $t\bar{t}$ events passing the dilepton selection and for the control sample. The identification of jets in the control sample is based on the measurable quantities.

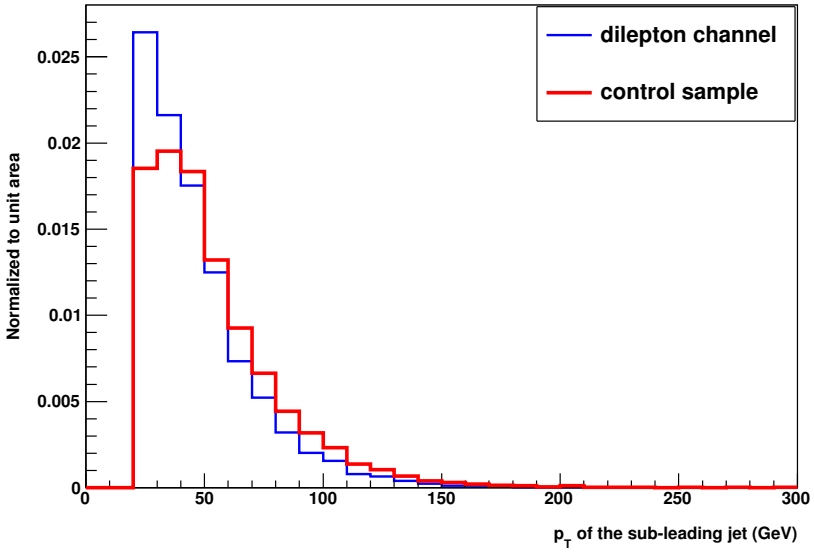

Figure 6.20: Distribution of p_T of the sub-leading jet for simulated $t\bar{t}$ events passing the dilepton selection and for the control sample. The identification of jets in the control sample is based on the measurable quantities. Only those events are compared which contain correct W jets.

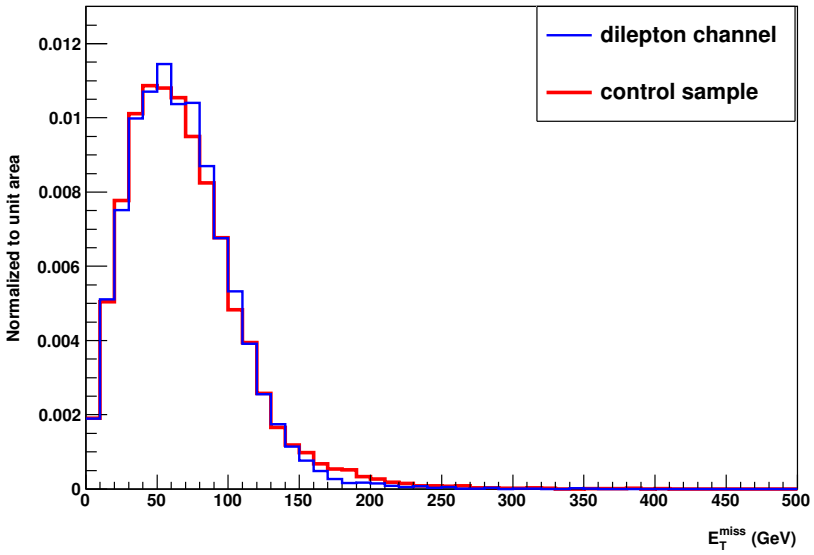

Figure 6.21: Distribution of E_T^{miss} for simulated $t\bar{t}$ events passing the dilepton selection and for the control sample. The identification of jets in the control sample is based on the measurable quantities.

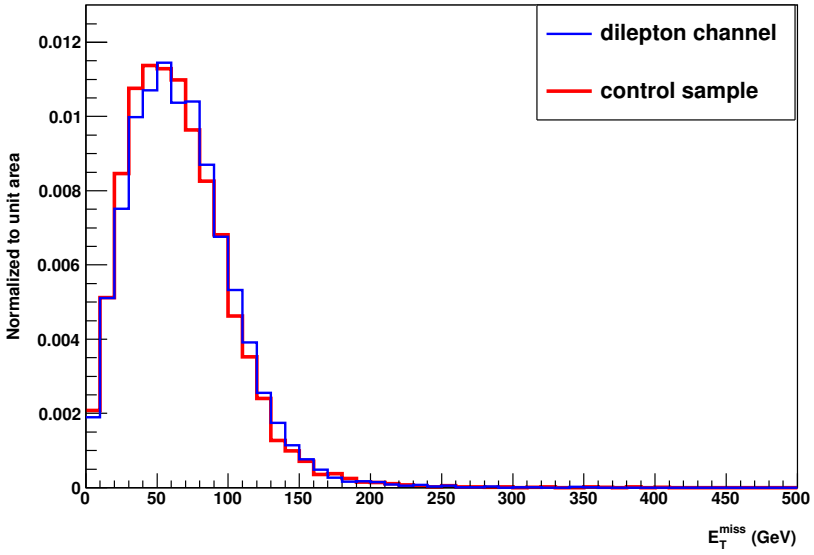

Figure 6.22: Distribution of E_T^{miss} for simulated $t\bar{t}$ events passing the dilepton selection and for the control sample. The identification of jets in the control sample is based on the measurable quantities. Only those events are compared which contain correct W jets.

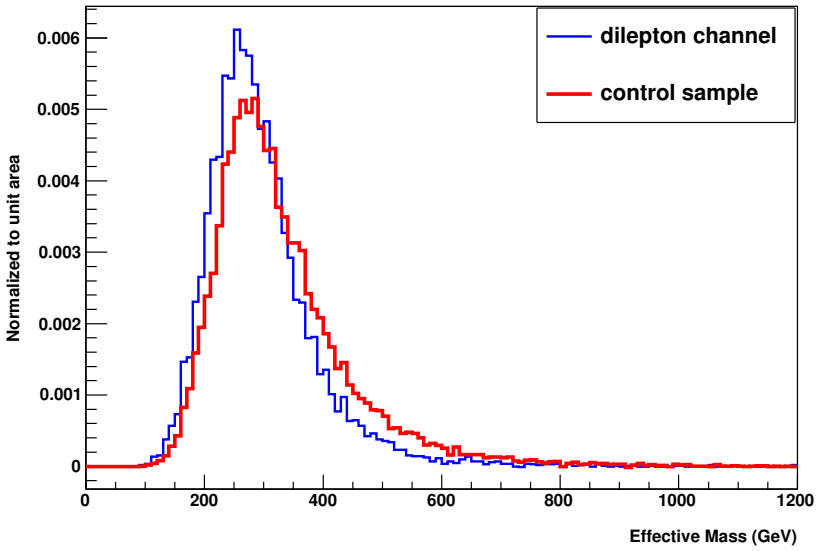

Figure 6.23: Distribution of M_{eff} for simulated $t\bar{t}$ events passing the dilepton selection and for the control sample. The identification of jets in the control sample is based on the measurable quantities.

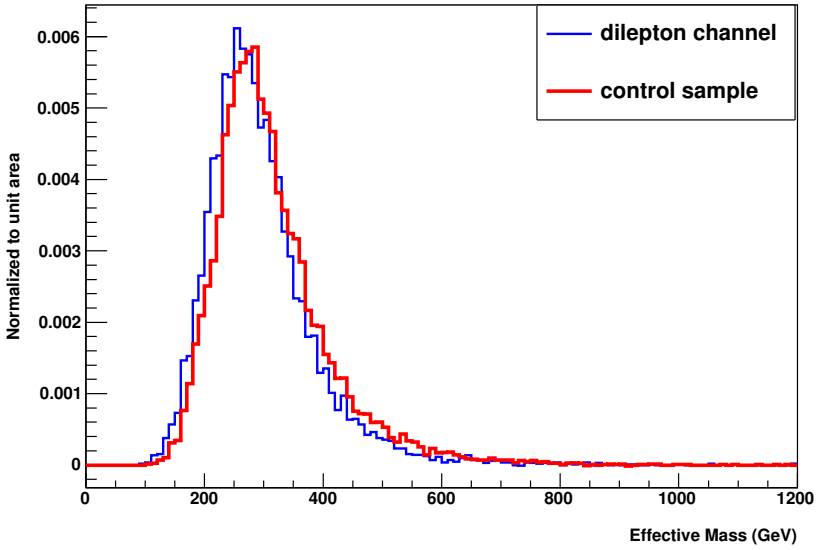

Figure 6.24: Distribution of M_{eff} for simulated $t\bar{t}$ events passing the dilepton selection and for the control sample. The identification of jets in the control sample is based on the measurable quantities. Only those events are compared which contain correct W jets.

6.5 Selection of $t\bar{t}$ Events

In the environment of mock and real data, other physics processes will also be present besides $t\bar{t}$. This means, when $4j + 1\ell$ events are selected for the $t\bar{t}$ control sample, non-$t\bar{t}$ events will also be accepted. Therefore, some procedure should be adopted to suppress those non-$t\bar{t}$ events. One way to achieve this is to construct a statistic that reflects the level of agreement between the event's measured characteristics and the $t\bar{t}$ hypothesis, and define a cut. Thus, the events that survive the cut are those that look like $t\bar{t}$. For the statistic we can write $\chi^2(q_1, q_2, b_1, b_2)$, i.e., the arguments represent, in the given order, the indices of the reconstructed jets assigned to q_1, q_2, b_1 and b_2 as shown in Figure 6.3. For the choice of the reconstructed jets a, b, c, d we can model the statistic as

$$\chi^2(a,b,c,d) = \frac{(m_{ab} - M_W)^2}{\sigma^2_{W_\mathrm{h}}} + \frac{(m_{abc} - m_t)^2}{\sigma^2_{t_\mathrm{h}}} + \frac{(m_{dl\nu} - m_t)^2}{\sigma^2_{t_\mathrm{l}}} - 2\ln\frac{L_W(w_a, w_b)}{f^{max}_{w_a} f^{max}_{w_b}} - 2\ln\frac{f(w_c|b)}{f^{max}_{w_c}} - 2\ln\frac{f(w_d|b)}{f^{max}_{w_d}} \tag{6.15}$$

where the variables have the same meaning as defined in Section 6.1 (Equations 6.1 - 6.4). Here, $f^{max}_{w_j}$ is the maximum of $[\, f(w_j|l), f(w_j|c), f(w_j|b)\,]$ where $j = a, b, c, d$. The first three terms correspond to the invariant masses of the hadronic W, the hadronic top and the leptonic top respectively. It is expected that the contribution of these mass terms in the above equation will be smaller for the $t\bar{t}$ events as compared to the non-$t\bar{t}$ events. While the last three terms in the chi-square provide the flavour tag information of the 4 reconstructed jets. Each $t\bar{t}$ decays into two b-jets that mostly have large flavour tag weights. It means, the last two terms in the above equation become nearly zero. Moreover, the above equation corresponds to the particular assignment of the reconstructed jets as shown in Figure 6.3 in which $q_1 = a$, $q_2 = b$, $b_1 = c$ and $b_2 = d$. There are 24 possible assignments, so we will compute 24 chi-square values,

and find which one is the minimum, i.e., χ^2_{min}. If we make a plot of the distribution of χ^2_{min} for $t\bar{t}$ events, we expect the distribution will move towards the lower values of χ^2_{min}. Four distributions of χ^2_{min}, each corresponding to specific physics process, are shown in Figure 6.25. It can be seen from the figure that W+jets is the most significant background, i.e., non-$t\bar{t}$ process, in the control sample. In Figure 6.25, the two peaks in the $t\bar{t}$ distribution are the characteristic of the $t\bar{t}$ events. The first peak on the left corresponds to the two b-jets which have large values of flavour tag weights. The second peak on the right corresponds to the case when one of the two b-jets has a lower value of flavour tag weight. The second peak can also be appeared when the $t\bar{t}$ control sample contains only one b-jet. In the light of the above, a cut value of χ^2_{min} is required to suppress the non-$t\bar{t}$ events. One can perform an optimisation study to find the best cut value. But for this thesis, a cut value of 5 is chosen by looking at the plot (Figure 6.25), which seems quite reasonable. That is only those events are accepted for the control sample if $\chi^2_{\text{min}} < 5$.

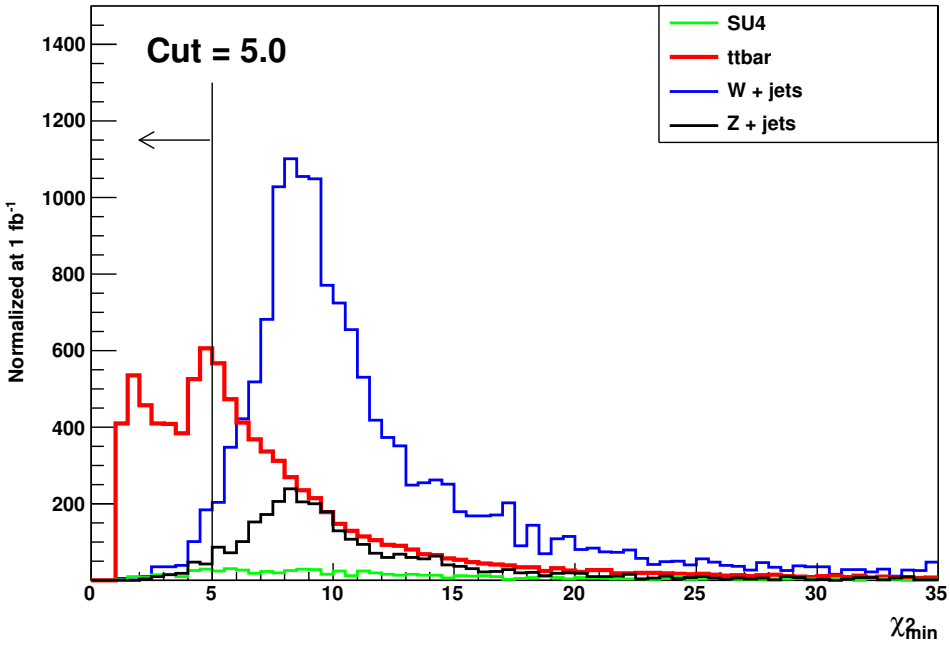

Figure 6.25: Selection of $t\bar{t}$ events.

Chapter 7

Results and Interpretation

The previous chapter served to provide the details of a novel, data-driven technique that we have developed for the estimation of the $t\bar{t}$ background. In this chapter, our aim is to test the above data driven method by using the mock data. This means, various physics processes will be considered that are relevant for the control and the dilepton search samples. Moreover, a C++ program has also been developed to compute the discovery significance of SUSY model (SU4) and upper limit on signal cross-section.

7.1 Estimating the $t\bar{t}$ Background using the Control Sample

We can now write down the full statistical procedure for the SUSY search. The statistical part of the analysis is mostly based on Ref [43]. In the $2j + 2l$ selection after all cuts we will find in data a certain number of events, n, which we model as following a Poisson distribution with an expectation value

$$E[n] = \mu s + b \; . \tag{7.1}$$

Here s is the expected number of events from the nominal signal model and μ is a

strength parameter defined so that $\mu = 0$ corresponds to the background-only hypothesis and $\mu = 1$ to the nominal signal hypothesis. By introducing the strength parameter it allows one to combine channels where one has different values of s but a common μ. The parameter b here refers specifically to the expected number of $t\bar{t}$ background events. In practice there will also be other sources of background but for purposes of the present discussion we assume they can be neglected. In this analysis, the non-$t\bar{t}$ backgrounds are estimated from Monte Carlo.

In the control sample ($4j + 1l$ selection), also from data (real or mock), we observe m events. This value is modelled as following a Poisson distribution with a mean

$$E[m] = \tau b \,, \tag{7.2}$$

where b is the expected number of background events in the $2j + 2l$ selection. That is, the b in Equation 7.2 for the control selection is the same as the expected background contributing to the $2j + 2l$ SUSY selection in Equation 7.1. Here, the scale factor τ relates the expected number of events found in the $4j + 1$ selection to the corresponding mean number in the $2j + 2l$ selection. Furthermore we assume that the scale factor τ in Equation 7.2 can be estimated by Equation 6.13 using the Monte Carlo.

The data thus consist of two measured values, n and m, and there are two unknown parameters, μ and b. Here μ is the parameter of interest and b is a nuisance parameter. In a more complete analysis, τ could also be regarded as nuisance parameter, but in the present study its value is taken to be fixed. For now we will treat s and τ as known parameters. The likelihood function for μ and b is the product of two Poisson terms:

$$L(\mu, b) = \frac{(\mu s + b)^n}{n!} e^{-(\mu s + b)} \, \frac{(\tau b)^m}{m!} e^{-\tau b} \,. \tag{7.3}$$

The log-likelihood function can therefore be written

$$\ln L(\mu, b) = n \ln(\mu s + b) - (\mu s + b) + m \ln(\tau b) - \tau b + C \,, \tag{7.4}$$

where the constant C represents terms that do not depend on the parameters and can be dropped.

Following Ref [43], to find the discovery significance, we define the test statistic q_0 as

$$q_0 = \begin{cases} -2 \ln \frac{L(0,\hat{\hat{b}})}{L(\hat{\mu},\hat{b})} & \hat{\mu} \geq 0 \\ 0 & \hat{\mu} < 0 \,. \end{cases} \tag{7.5}$$

To set an upper limit on a hypothesized value of the strength parameter μ, we define the test statistic q_μ as

$$q_\mu = \begin{cases} -2 \ln \frac{L(\mu,\hat{\hat{b}})}{L(\hat{\mu},\hat{b})} & \hat{\mu} \leq \mu \\ 0 & \hat{\mu} > \mu \,. \end{cases} \tag{7.6}$$

Here $\hat{\mu}$ and $\hat{b}$ are the values of the parameters that maximize the likelihood (the ML estimators), and $\hat{\hat{b}}$ is the value of b that maximises L for the given μ (the conditional ML estimator).

If there is only one background process, then the estimators for μ and b can be found by setting the corresponding derivatives of $\ln L$ equal to zero. One finds:

$$\hat{\mu} = \frac{n - m/\tau}{s} \,, \tag{7.7}$$

$$\hat{b} = \frac{m}{\tau} \,. \tag{7.8}$$

The conditional ML estimator $\hat{\hat{b}}$ for a specified μ is

$$\hat{\hat{b}} = \frac{n + m - (1+\tau)\mu s}{2(1+\tau)} + \left[\frac{(n + m - (1+\tau)\mu s)^2 + 4(1+\tau)m\mu s}{4(1+\tau)^2} \right]^{1/2} \tag{7.9}$$

Equations (7.6), (7.7), (7.8), (7.9) can be combined to give a value of q_μ for given data values n and m. In cases with more than one background component, it is easiest to solve for the required quantities numerically. A program for doing this has been developed in this thesis.

One can show that for sufficiently large n and m, the sampling distribution of q_μ under the hypothesis of μ is a combination of a delta function at zero and a chi-square distribution for one degree of freedom, with each component having weight one half. We call this the half-chi-square distribution.

Using this information one can compute for a value of q_μ the p-value of the hypothesis μ,

$$p_\mu = \int_{q_{\mu,\mathrm{obs}}}^{\infty} f(q_\mu|\mu)\, dq_\mu \ , \tag{7.10}$$

and from this one can find the corresponding significance

$$Z_\mu = \Phi^{-1}(1 - p_\mu) \ , \tag{7.11}$$

where Φ is the cumulative standard Gaussian distribution (zero mean and unit width), and Φ^{-1} is its inverse (the quantile). In order to establish a discovery we try to reject the background-only hypothesis $\mu = 0$. For example, a threshold significance of $Z = 5$ corresponds to a p-value of 2.87×10^{-7}. While for computing the upper limit on μ at 95 % confidence level, a p-value of 0.05 corresponds to a significance of $Z = 1.64$.

For the half-chi-square distribution for $f(q_0|q_0)$ and $f(q_\mu|q_\mu)$, one finds that the discovery and exclusion significances are given respectively by the simple formulas

$$Z_0 = \sqrt{q_0}\ , \tag{7.12}$$

and

$$Z_\mu = \sqrt{q_\mu}\ . \tag{7.13}$$

In the preparation of an analysis, one often needs the expected (or median) significance. For the discovery, one can report the expected significance one would obtain for data containing signal plus background. While for purposes of upper limits, one usually wants the median significance with which one would exclude $\mu = 1$, where the data distribution for obtaining the median assumes background only.

To find the median significance, one can evaluate q_μ (and q_0) using an artificial data set where n and m are replaced by their expectation values $\mu' s + b$ and τb, respectively (called the *Asimov data set*). Here μ' is the value of the strength parameter corresponding to data distribution one wants for the median. For discovery significance, one wants $\mu' = 1$, i.e., the signal plus background. While for upper limits one wants $\mu' = 0$, i.e., the background-only hypothesis.

7.2 Preparation of Mock Data

In order to estimate $t\bar{t}$ background, we need to determine the value of the scale factor τ which we introduced in the previous chapter. The $t\bar{t}$ event survival rates with an effective luminosity L_{MC} of $8.8\,\mathrm{fb}^{-1}$ are given in Table 7.1. This result is based on fully simulated data. The sets of cuts designated Cut2, Cut3 and Cut4 are the same as defined in Section 5.2.1. The scale factor τ can be estimated by using Equation 6.13, i.e., $\tau = 139/38 \approx 3.7$.

In addition to the scale factor, we also need to know the following information: events expected in the signal region (SR), $E[n]$, events expected in the control region (CR),

Cross-Section (pb)	L_{MC} (fb^{-1})	Event Selection	Cut2	Cut3	Cut4
80.03	8.8	$2j + 2\ell$	757	51	38
80.03	8.8	$4j + 1\ell$	3664	180	139

Table 7.1: Number of $t\bar{t}$ events at various selection cuts in the search and control samples.

Quantities	Value
events expected in the SR, $E[n]$	14.32
events expected in the CR, $E[m]$	16.1
expected signal events, s	9.58
expected non-$t\bar{t}$ events in the SR, $b_{\text{non}-t\bar{t}-\text{SR}}$	0.44
expected non-$t\bar{t}$ events in the CR, $b_{\text{non}-t\bar{t}-\text{CR}}$	0.2
expected $t\bar{t}$ events in the SR, $b_{t\bar{t}}$	4.3
expected $t\bar{t}$ events in the CR, $\tau b_{t\bar{t}}$	15.9

Table 7.2: Some useful data at the integrated luminosity of $1\,\text{fb}^{-1}$.

$E[m]$, expected signal events, s, non-$t\bar{t}$ events expected in the SR, $b_{\text{non}-t\bar{t}-\text{SR}}$, non-$t\bar{t}$ events expected in the CR, $b_{\text{non}-t\bar{t}-\text{SR}}$, expected $t\bar{t}$ events in the SR, $b_{t\bar{t}}$, and expected $t\bar{t}$ events in the CR, $\tau b_{t\bar{t}}$. These quantities are determined using fully simulated data of the physics processes relevant for the search and the control sample, and their values are listed in Table 7.2.

To compute discovery significance and upper limit, one needs to determine the values of n and m (defined in Section 7.1). In order to do so, the physics processes we saw in Chapter 5 have been combined into one data sample (called mock data) with an integrated luminosity of $0.5\,\text{fb}^{-1}$. The mock data events observed in the signal and control regions are listed in Tables 7.3 and 7.4 respectively. Here, the different cut levels have their usual meanings. After all the cuts, the number of events that survived in the dilepton search and in the control samples are 9 and 5 respectively, i.e., $n = 9$ and $m = 5$.

Sample	2 jets + 2 leptons	Cut2	Cut3	Cut4
mock data	15588	352	9	9
SU4	29	11	6	6
$t\bar{t}$	266	53	3	3
diboson	76	0	0	0
Drell Yan	507	3	0	0
W+jets	66	4	0	0
Z+jets	14644	281	0	0

Table 7.3: Search sample events observed in mock data at 0.5 fb^{-1}.

Sample	4 jets + 1 lepton	Cut2	Cut3	Cut4
mock data	2030	300	10	5
SU4	57	6	0	0
$t\bar{t}$	1008	201	7	5
diboson	9	1	0	0
Drell Yan	18	0	0	0
W+jets	691	76	3	0
Z+jets	247	16	0	0

Table 7.4: Control sample events observed in mock data at 0.5 fb^{-1}.

Quantities	Value
n, events observed in the SR	9
m, events observed in the CR	5

Table 7.5: Events observed in mock data sample at 0.5 fb^{-1}.

7.3 Discovery Significance and Upper Limit

In Section 7.1, we wrote full statistical procedure for the SUSY dilepton search. In this connection, a C++ program called *LimitCalc* has been developed to compute the discovery significance and upper limit. The LimitCalc program is a modified version of SigCalc [44] program which was developed for computing the discovery significance. The measurements obtained from the mock data are listed in Table 7.5.

7.3.1 Discovery Significance

We have implemented two ways to estimate the discovery significance Z_0. In the first method, we compute the statistic q_0 for the measured values n and m listed in Table 7.5 by using Equation 7.5. It is pointed out earlier that if the distribution of q_0 follows the half-chi-square distribution (asymptotic), then one can compute the discovery significance by using Equation 7.12, i.e., $Z_0 = \sqrt{q_0} = 3.35$. The asymptotic formula is valid for the large data sample.

If the data sample is not large enough to guarantee the validity of the asymptotic formula, one can use Monte Carlo experiments to find the distribution of q_0. In this method, the measurements (n and m) are generated after setting $\mu = 0$ as

$$n_{\text{gen}} \sim \text{Poisson}(b_{t\bar{t}} + b_{\text{non}-t\bar{t}-\text{SR}}) \tag{7.14}$$

$$m_{\text{gen}} \sim \text{Poisson}(\tau b_{t\bar{t}} + b_{\text{non}-t\bar{t}-\text{CR}}) \tag{7.15}$$

where the variables have their usual meanings. In the first method, we had only one set

of measurements, and from this we found $q_0(n, m)$, which we now call $q_{0,\text{obs}}$. But in the second method, we have the distributions of measurements. This means, for each value of n_{gen} and m_{gen}, one can obtain a value of the statistic q_0. Therefore, one can make the distribution of q_0 by using all the values of n_{gen} and m_{gen}. Later, one can compute the p-value (called p_0) as

$$p_0 = \frac{\text{number of MC experiments when } \; q_0 > q_{0,\text{obs}}}{\text{total number of MC experiments}} \tag{7.16}$$

Finally, the discovery significance is computed by $Z_0 = \Phi^{-1}(1 - p_0)$ (Equation 7.11), and it is found to be 3.30, in good agreement with the value of 3.35 based on the assymptotic formula. This result can also be confirmed by looking at Figure 7.1. In this figure, the red line corresponds to the half-chi-square distribution, while the blue histogram represents the distribution of q_0 made by using the values of n_{gen} and m_{gen}. One can see from Figure 7.1 that the two distributions are in good agreement, which is equivalent to the statement that the significance, which corresponds to the area under the curve to the right of $q_{0,\text{obs}}$, is essentially the same.

We have seen two ways to estimate the discovery significance Z_0 for the data sets (n,m) and (n_{gen},m_{gen}). Now we want to know what would be the distribution of Z_0 if one were to obtain many independent data sets, each generated according to: $n_{\text{gen}} \sim \text{Poisson}(\mu s + b_{t\bar{t}} + b_{\text{non}-t\bar{t}-\text{SR}})$ and $m_{\text{gen}} \sim \text{Poisson}(\tau b_{t\bar{t}} + b_{\text{non}-t\bar{t}-\text{CR}})$. In particular, we want to know the expected (or median) discovery significance if the data are generated using $\mu = 1$. This is our measure of experimental sensitivity. The distribution of Z_0 is shown in Figure 7.2. One way to find the expected discovery significance is by using Asimov data set as pointed out in Section 7.1. From the MC, construct the Asimov data set as

$$n_{A,1} = s + b_{t\bar{t}} + b_{\text{non}-t\bar{t}-\text{SR}} = 7.16 \tag{7.17}$$

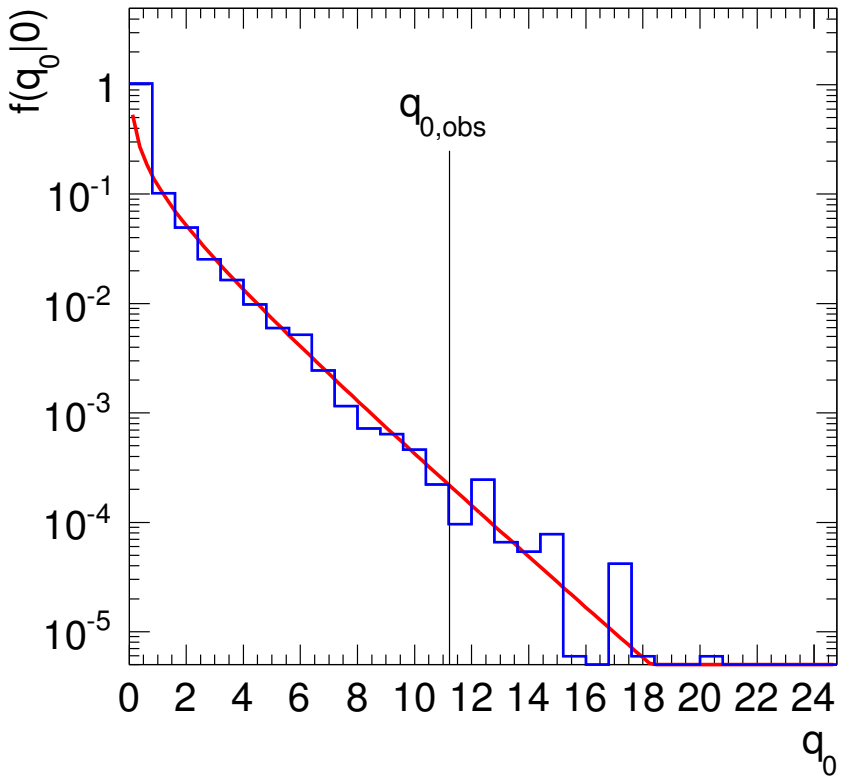

Figure 7.1: The comparison of Monte Carlo and $\frac{1}{2}\chi^2$ distributions.

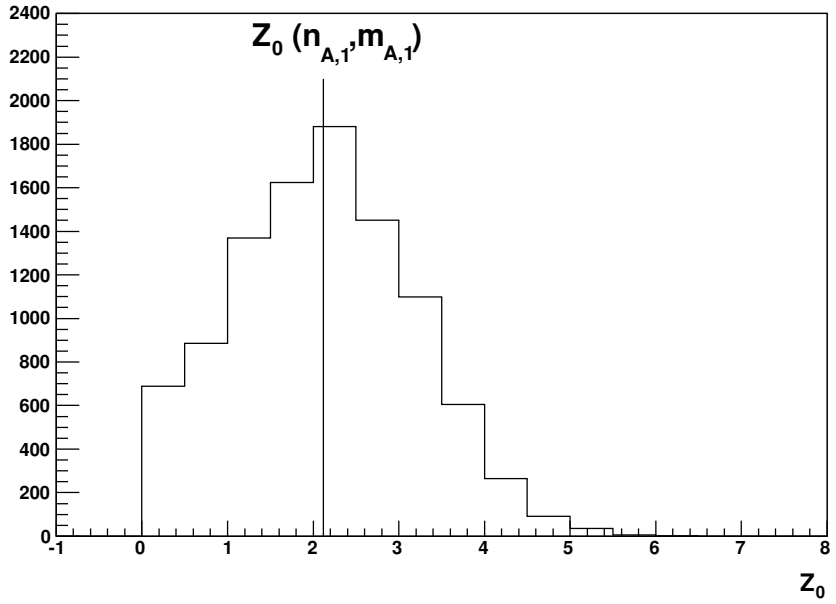

Figure 7.2: Distribution of discovery significance Z_0 for many independent data sets. The expected significance $Z_0(n_{A,1}, m_{A,1})$ is also shown.

$$m_{A,1} = \tau b_{t\bar{t}} + b_{\text{non}-t\bar{t}-\text{CR}} = 8.05 \tag{7.18}$$

where the variables have their usual meanings. By using the first method above, the expected discovery significance is found to be $Z_0(n_{A,1}, m_{A,1}) = \sqrt{q_0(n_{A,1}, m_{A,1})} = 2.1$, which is also shown in Figure 7.2.

7.3.2 Upper Limit

In addition to estimate the discovery significance, one also needs to know the upper limit on the strength parameter μ. That is one wants to compute the maximum value of μ that corresponds to the p-value of 0.05 (95 % confidence level CL). In this connection, we have implemented three ways to find the upper limit μ_{up}. Two of them use the asymptotic approach, which is only valid for the large data set, while one method is based on the Monte Carlo study.

This method is based on the asymptotic approximation which means it is valid for sufficiently large data set. Here, the upper limit μ_{up} at 95 % CL is computed by

$$\mu_{\text{up}} = \hat{\mu} + 1.64\,\sigma_{\hat{\mu}}, \tag{7.19}$$

where $\sigma_{\hat{\mu}}$ is the standard deviation, and the other variables have their usual meanings. The estimate of $\hat{\mu}$ and $\sigma_{\hat{\mu}}$ are obtained from the fit. For the measurements listed in Table 7.5, i.e., $n = 9$ and $m = 5$, the estimated values of $\hat{\mu}$ and $\sigma_{\hat{\mu}}$ are 1.55 and 0.64 respectively. By using the above equation, the upper limit is found to be 2.6.

Like above, this method also uses the asymptotic approach. But here, we test various values of μ in some range (e.g. $0 \leq \mu \leq 3$), and then the maximum value of μ is found by using a graph. In this method, we compute the statistic q_μ by using Equation 7.6. Although, the measurements n and m are fixed at 9 and 5 respectively, but q_μ will be different because of the variation of μ in the range $(0 \leq \mu \leq 3)$. That is we have a value of q_μ, which we call $q_{\mu,\text{obs}}$, for each value of μ. Later, a list of p_μ values can be formed by using $p_\mu = 1 - \Phi(\sqrt{q_{\mu,\text{obs}}})$ corresponding to the values of the statistic $q_{\mu,\text{obs}}$. Here, Φ is the cumulative standard Gaussian distribution (zero mean and unit width). Finally, a plot of p_μ is made against μ, and the largest μ is computed at 95 % CL. The plot is shown in Figure 7.3, and the upper limit μ_{up} from this graph is found to be about 2.8, i.e., the value of μ at $p_\mu = 0.05$.

If the data sample is not large enough to guarantee the validity of the asymptotic formula, one can use Monte Carlo experiments to find the distribution of q_0. In this method, the measurements n and m are generated after setting $\mu = 1$ as

$$n_{\text{gen}} \sim \text{Poisson}(s + b_{t\bar{t}} + b_{\text{non}-t\bar{t}-\text{SR}}) \tag{7.20}$$

$$m_{\text{gen}} \sim \text{Poisson}(\tau b_{t\bar{t}} + b_{\text{non}-t\bar{t}-\text{CR}}) \tag{7.21}$$

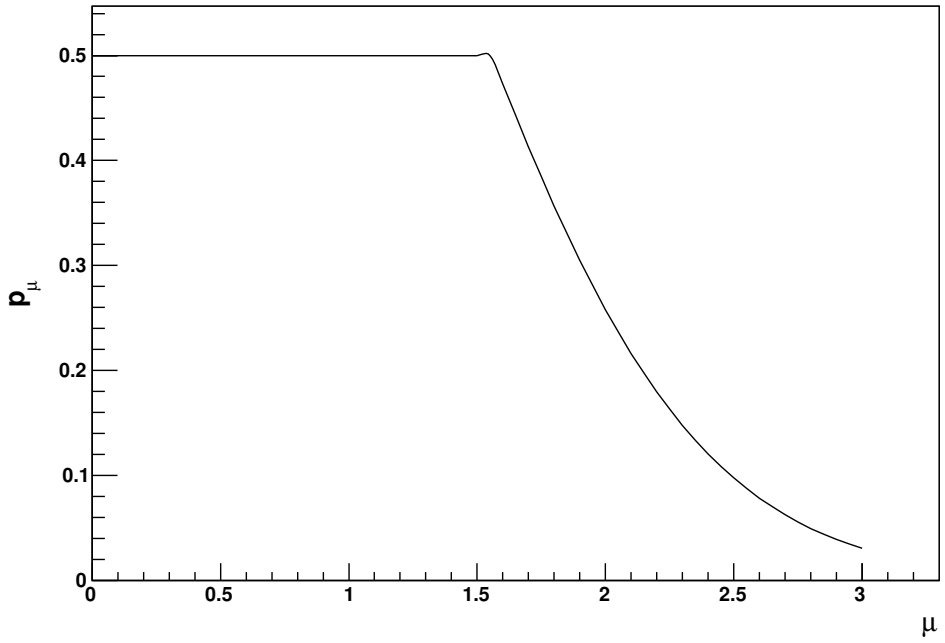

Figure 7.3: Plot of p_μ against μ based on the asymptotic formula.

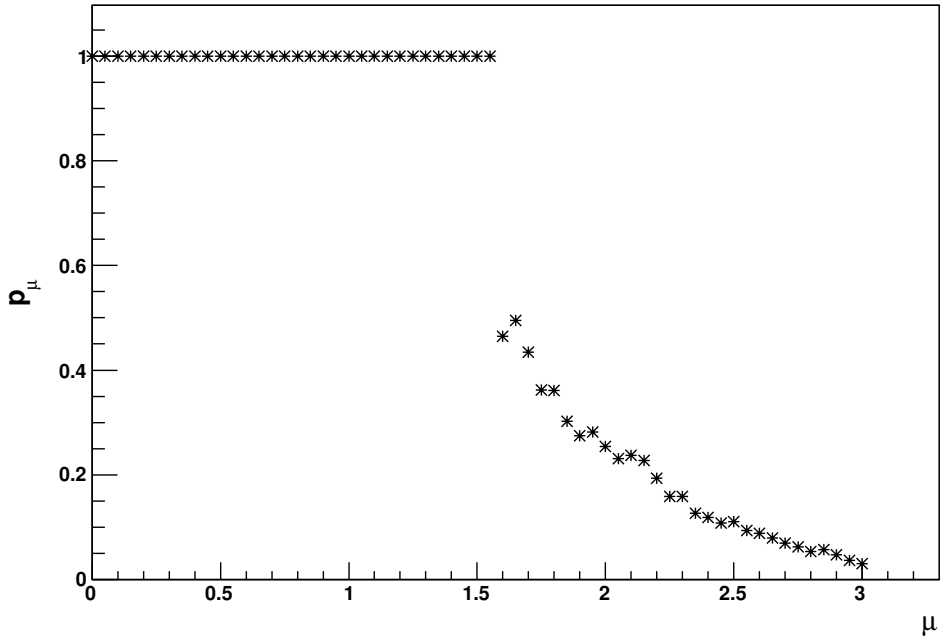

Figure 7.4: Plot of p_μ against μ based on the Monte Carlo experiments.

where the variables have their usual meanings. For each value of n_{gen}, m_{gen} and μ, one can compute a value of q_μ. Next, one needs to make a list of p_μ corresponding to the μ values in the range $0 \leq \mu \leq 3$ as

$$p_\mu = \frac{\text{number of MC experiments when } \; q_\mu > q_{\mu,\text{obs}}}{\text{total number of MC experiments}} \tag{7.22}$$

Like the second method above, we make a plot of p_μ against μ, and then compute μ that corresponds to 95% CL. The plot is shown in Figure 7.4 and the upper limit from this graph is found to be about 2.9, in reasonably good agreement with the value of 2.8 based on the assymptotic formula (Figure 7.3).

We have seen three ways to estimate the upper limit μ_{up}. Now we want to know what would be the distribution of the limits μ_{up} if one were to obtain many independent data sets, each generated according to: $n_{\text{gen}} \sim \text{Poisson}(\mu s + b_{t\bar{t}} + b_{\text{non}-t\bar{t}-\text{SR}})$ and

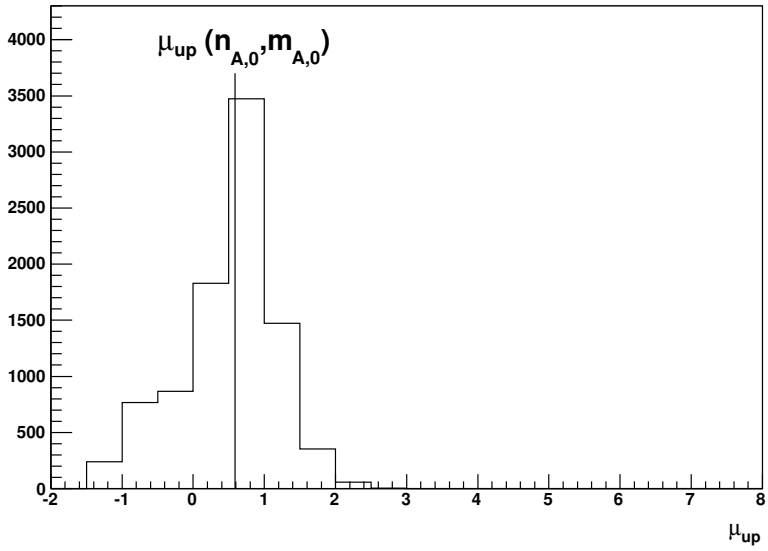

Figure 7.5: Distribution of upper limit μ_{up} for many independent data sets. The expected upper limit $\mu_{\text{up}}(n_{A,0}, m_{A,0})$ is also shown.

$m_{\text{gen}} \sim \text{Poisson}(\tau b_{t\bar{t}} + b_{\text{non}-t\bar{t}-\text{CR}})$. In particular, we want to know the expected (or median) upper limit if the data are generated using $\mu = 0$. This is our measure of experimental sensitivity, i.e., the limit we expect to set if there is no signal present in nature. The distribution of μ_{up} is shown in Figure 7.5. One way to find the expected upper limit is by using Asimov data set as pointed out in Section 7.1. From the MC, construct the Asimov data set as

$$n_{A,0} = b_{t\bar{t}} + b_{\text{non}-t\bar{t}-\text{SR}} = 2.37 \tag{7.23}$$

$$m_{A,0} = \tau b_{t\bar{t}} + b_{\text{non}-t\bar{t}-\text{CR}} = 8.05 \tag{7.24}$$

where the variables have their usual meanings. By using the first method above, the expected upper limit $\mu_{\text{up}}(n_{A,0}, m_{A,0})$ is found to be 0.59, which is also shown in Figure 7.5.

7.4 Treatment of Uncertainty in Scale Factor τ

The uncertainty in the scale factor τ can be modeled with a log-normal distribution or equivalently with Gaussian pdf as

$$f(\eta_1; \eta, \sigma_{\eta_1}) = \frac{1}{\sqrt{2\pi}\,\sigma_{\eta_1}} \exp\left(-\frac{(\eta_1 - \eta)^2}{2\sigma_{\eta_1}^2}\right) \tag{7.25}$$

where $\eta_1 = \ln \tau_1$ and $\eta = \ln \tau$. Here, τ_1 is unknown and it will be treated as a nuisance parameter, while τ is the scale factor whose value is calculated earlier, i.e., 3.7. The standard deviation σ_{η_1} is defined as

$$\sigma_{\eta_1} = \ln(1 + \sigma_{\text{rel}}) \tag{7.26}$$

where σ_{rel} is the relative uncertainty in scale factor and one can take its value to be 0.1, 0.2 or 0.5. The likelihood function for μ and b along with the uncertainty in scale factor can be written as

$$L(\mu, b, \tau_1) = \frac{(\mu s + b)^n}{n!} e^{-(\mu s + b)}\, \frac{(\tau b)^m}{m!} e^{-\tau b}\, \frac{1}{\sqrt{2\pi}\,\sigma_{\eta_1}} \exp\left(-\frac{(\eta_1 - \eta)^2}{2\sigma_{\eta_1}^2}\right) . \tag{7.27}$$

where the first two terms are the same as in Equation 7.3, while the third term modeled the uncertainty in scale factor. All variables have their usual meanings. Now repeat the steps followed in Sections 7.1 and 7.3, and determine again the sensitivity, i.e., median significance. The result will indicate how an uncertainty in scale factor would affect the experimental sensitivity.

Chapter 8

Conclusions and Outlook

The main theme of this thesis was to design a search for Supersymmetry in ATLAS by requiring events with two opposite-sign leptons, two jets and missing transverse energy in the final state. We have seen various Standard Model processes which also contain the above kinematics, and these are background to a SUSY signal. The $t\bar{t}$ process is the most dominant background in the signal region. Before one claims a SUSY discovery, the proper understanding of these backgrounds is essential. Therefore, data driven methods are used to estimate these backgrounds.

A novel data driven technique for estimating the $t\bar{t}$ background has been presented in this thesis. To constrain the $t\bar{t}$ events, control sample has been prepared with $4j + 1\ell$ selection. The correct identification of W jets was a challenging task, which has been done by choosing the jet assignment with the maximum likelihood and in addition, requiring probability of W jets assignment exceeds a given threshold. This probability is not as high as one might hope, because the 2 W jets survived the selection cuts only 59 % of the cases. When the 2 W jets are accepted in the control sample, the method identifies them 87 % correctly. Moreover, the distributions from $t\bar{t}$ in the $2j+2\ell$ selection (dilepton search sample) to those from $t\bar{t}$ in the $4j + 1\ell$ selection (control sample) are compared, and it has been found that the distribution shapes are strongly dependent on

the correct identification of the 2 W jets.

The analysis has been tested using simulated data with an integrated luminosity of $0.5\,\mathrm{fb}^{-1}$. A statistical analysis based on the profile-likelihood method has been developed for the search. It has been seen that although the number of events is quite small, the significance from asymptotic formulae are in reasonably good agreement with values obtained from Monte Carlo. For a data sample of $0.5\,\mathrm{fb}^{-1}$, the median discovery significance for the benchmark point SU4 in the mSUGRA parameter space was found to be 2.1. Assuming the absence of a SUSY signal, the median upper limit on the cross section for SUSY (SU4) is 0.59 times the predicted cross section, which is to say one would expect to exclude this model.

A possible extension to the work presented in this thesis may be to relax the cuts on pseudorapidity $|\eta|$ and transverse momentum p_T of jets, and to require four or more jets in the control sample, so that the acceptance fraction of the 2 W jets is significantly higher than 0.59.

SUSY Dilepton Search in ATLAS

The analysis overview of SUSY dilepton search was given in Chapter 5, which was mostly based on ATLAS dilepton note [1]. The recent publication in ATLAS on this channel is Ref [45]. The recent analysis uses a data sample collected during the first half of 2011 that corresponds to a total integrated luminosity of $1.0\,\mathrm{fb}^{-1}$ recorded with the ATLAS detector. The aim of this section is to discuss some of the main results of this publication.

In 2011 analysis, three signal regions are considered, placing requirements on E_T^{miss} and number of high p_T jets, as shown in Table 8.1. These regions are optimised by considering their potential reach in the parameter space of mSUGRA/CMSSM [46], [47] models. These models have varying mass parameters m_o and $m_{\frac{1}{2}}$, but fixed values of $A_o = 0$, $\tan\beta = 10$ and $\mathrm{sign}(\mu) > 0$.

The expected and observed number of events in each signal region are compared

Signal Region	OS-SR1	OS-SR2	OS-SR3
E_T^{miss} [GeV]	250	220	100
Leading jet p_T [GeV]	-	80	100
Second jet p_T [GeV]	-	40	70
Third jet p_T [GeV]	-	40	70
Fourth jet p_T [GeV]	-	-	70
Number of jets	-	≥ 3	≥ 4

Table 8.1: Criteria defining each of the three signal regions for opposite-sign (OS-SRx) analysis [45].

	Background	Observed	95% CL
OS-SR1	15.5 $\pm$ 4.0	13	9.9 fb
OS-SR2	13.0 $\pm$ 4.0	17	14.4 fb
OS-SR3	5.7 $\pm$ 3.6	2	6.4 fb

Table 8.2: Predicted number of background events, observed number of events and the corresponding 95% CL upper limit on $\sigma \times \epsilon \times A$, using the CL_s technique for each signal region [45].

to the background expectation as shown in Table 8.2. It can be seen from Table 8.2, there is a good agreement between the numbers of observed events and the Standard Model predictions. These results are used to set limits on the effective production cross-section, i.e., $\sigma \times \epsilon \times A$. Here, σ is the cross-section for new phenomena, ϵ is the detector reconstruction and identification efficiency, while A is the fraction of events passing geometric and kinematic cuts at particle level. Limits are set using the CL_s prescription, as described in Ref [48]. The results on limits are also shown in Table 8.2. Effective production cross-sections in excess of 9.9 fb for events containing supersymmetric particles with E_T^{miss} greater than 250 GeV are excluded at 95% CL.

Appendix A

Data Samples

The following ATLAS samples were used for the dilepton search analysis described in this thesis:

mc10_7TeV.106400.SU4_jimmy_susy.merge.AOD.e598_s933_s946_r2175_r2176

mc10_7TeV.105200.T1_McAtNlo_Jimmy.merge.AOD.e598_s933_s946_r2215_r2260

mc10_7TeV.105985.WW_Herwig.merge.AOD.e598_s933_s946_r2215_r2260

mc10_7TeV.105986.ZZ_Herwig.merge.AOD.e598_s933_s946_r2215_r2260

mc10_7TeV.105987.WZ_Herwig.merge.AOD.e598_s933_s946_r2215_r2260

mc10_7TeV.108319.PythiaDrellYan_mumu.merge.AOD.e574_s933_s946_r2215_r2260

mc10_7TeV.108320.PythiaDrellYan_ee.merge.AOD.e574_s933_s946_r2215_r2260

mc10_7TeV.108321.PythiaDrellYanLowM_mu3.merge.AOD.e574_s933_s946_r2215_r2260

mc10_7TeV.108322.PythiaDrellYanLowM_ee3.merge.AOD.e574_s933_s946_r2215_r2260

mc10_7TeV.107680.AlpgenJimmyWenuNp0_pt20.merge.AOD.e600_s933_s946_r2215_r2260

mc10_7TeV.107681.AlpgenJimmyWenuNp1_pt20.merge.AOD.e600_s933_s946_r2215_r2260

mc10_7TeV.107682.AlpgenJimmyWenuNp2_pt20.merge.AOD.e760_s933_s946_r2215_r2260

mc10_7TeV.107683.AlpgenJimmyWenuNp3_pt20.merge.AOD.e760_s933_s946_r2215_r2260

mc10_7TeV.107684.AlpgenJimmyWenuNp4_pt20.merge.AOD.e760_s933_s946_r2215_r2260

mc10_7TeV.107685.AlpgenJimmyWenuNp5_pt20.merge.AOD.e760_s933_s946_r2215_r2260

mc10_7TeV.107690.AlpgenJimmyWmunuNp0_pt20.merge.AOD.e600_s933_s946_r2215_r2260

mc10_7TeV.107691.AlpgenJimmyWmunuNp1_pt20.merge.AOD.e600_s933_s946_r2215_r2260

mc10_7TeV.107692.AlpgenJimmyWmunuNp2_pt20.merge.AOD.e760_s933_s946_r2215_r2260

mc10_7TeV.107693.AlpgenJimmyWmunuNp3_pt20.merge.AOD.e760_s933_s946_r2215_r2260

mc10_7TeV.107694.AlpgenJimmyWmunuNp4_pt20.merge.AOD.e760_s933_s946_r2215_r2260

mc10_7TeV.107695.AlpgenJimmyWmunuNp5_pt20.merge.AOD.e760_s933_s946_r2215_r2260

mc10_7TeV.107700.AlpgenJimmyWtaunuNp0_pt20.merge.AOD.e600_s933_s946_r2215_r2260

mc10_7TeV.107701.AlpgenJimmyWtaunuNp1_pt20.merge.AOD.e600_s933_s946_r2215_r2260

mc10_7TeV.107702.AlpgenJimmyWtaunuNp2_pt20.merge.AOD.e760_s933_s946_r2215_r2260

mc10_7TeV.107703.AlpgenJimmyWtaunuNp3_pt20.merge.AOD.e760_s933_s946_r2215_r2260

mc10_7TeV.107704.AlpgenJimmyWtaunuNp4_pt20.merge.AOD.e760_s933_s946_r2215_r2260

mc10_7TeV.107705.AlpgenJimmyWtaunuNp5_pt20.merge.AOD.e760_s933_s946_r2215_r2260

mc10_7TeV.107650.AlpgenJimmyZeeNp0_pt20.merge.AOD.e737_s933_s946_r2215_r2260

mc10_7TeV.107651.AlpgenJimmyZeeNp1_pt20.merge.AOD.e737_s933_s946_r2215_r2260

mc10_7TeV.107652.AlpgenJimmyZeeNp2_pt20.merge.AOD.e737_s933_s946_r2215_r2260

mc10_7TeV.107653.AlpgenJimmyZeeNp3_pt20.merge.AOD.e737_s933_s946_r2215_r2260

mc10_7TeV.107654.AlpgenJimmyZeeNp4_pt20.merge.AOD.e737_s933_s946_r2215_r2260

mc10_7TeV.107655.AlpgenJimmyZeeNp5_pt20.merge.AOD.e737_s933_s946_r2215_r2260

mc10_7TeV.107660.AlpgenJimmyZmumuNp0_pt20.merge.AOD.e737_s933_s946_r2215_r2260

mc10_7TeV.107661.AlpgenJimmyZmumuNp1_pt20.merge.AOD.e737_s933_s946_r2215_r2260

mc10_7TeV.107662.AlpgenJimmyZmumuNp2_pt20.merge.AOD.e737_s933_s946_r2215_r2260

mc10_7TeV.107663.AlpgenJimmyZmumuNp3_pt20.merge.AOD.e737_s933_s946_r2215_r2260

mc10_7TeV.107664.AlpgenJimmyZmumuNp4_pt20.merge.AOD.e737_s933_s946_r2215_r2260

mc10_7TeV.107665.AlpgenJimmyZmumuNp5_pt20.merge.AOD.e737_s933_s946_r2215_r2260

mc10_7TeV.107670.AlpgenJimmyZtautauNp0_pt20.merge.AOD.e737_s933_s946_r2215_r2260

mc10_7TeV.107671.AlpgenJimmyZtautauNp1_pt20.merge.AOD.e737_s933_s946_r2215_r2260

mc10_7TeV.107672.AlpgenJimmyZtautauNp2_pt20.merge.AOD.e737_s933_s946_r2215_r2260

mc10_7TeV.107673.AlpgenJimmyZtautauNp3_pt20.merge.AOD.e737_s933_s946_r2215_r2260

mc10_7TeV.107674.AlpgenJimmyZtautauNp4_pt20.merge.AOD.e737_s933_s946_r2215_r2260

mc10_7TeV.107675.AlpgenJimmyZtautauNp5_pt20.merge.AOD.e737_s933_s946_r2215_r2260

The Monte Carlo generators used for the production of the above data samples are listed in Table 5.1, Table 5.2 and Table 5.3. These data samples are centrally produced that fully simulate the ATLAS detector using GEANT4 package [31]. They are analysed using Athena release 16.

Bibliography

[1] The ATLAS Collaboration. *"SUSY Searches with Dileptons and High Missing Transverse Momentum, Tech. Rep."*. ATL–PHYS–INT–2011–030, CERN, Geneva, 2011.

[2] D. Griffiths. *Introduction to Elementary Particles*. John Wiley and Sons, 1987.

[3] D. Green. *High P_T Physics at Hadron Colliders*. Cambridge University Press, 2005.

[4] C. Quigg. *Gauge Theories of the Strong, Weak and Electromagnetic Interactions*. Benjamin–Cummings Publishing Company, 1983.

[5] K. Nakamura et. al. *"Particle Data Group"*. J. Phys. G37 075021, 2010.

[6] Y. Fukada et. al. *"Evidence for Oscillations of Atmospheric Neutrinos"*. Phys. Rev. Lett. 81, (1998) 1562–1567.

[7] The SNO Collaboration. *"Independent Measurement of the Total Active* ^{8}B *Solar Neutrino Flux Using an Array of* ^{3}He *Proportional Counters at the Sudbury Neutrino Observatory"*. Phys. Rev. Lett. 101, (2008).

[8] The Super-Kamiokande Collaboration. *"Solar neutrino measurements in Super–Kamiokande-II"*. Phys. Rev. D78, (2008).

[9] G. Kane. *"The Mysteries of Mass"*. Sci. Am., (July 2005).

[10] LEP Higgs Working Group. http://lephiggs.web.cern.ch/LEPHIGGS/papers/July2002_SM/index.html.

[11] The Tevatron New-Phenomena and Higgs Working Group. http://tevnphwg.fnal.gov/results/SM_Higgs_Summer_11/,arXiv:hep-ex/1107.5518(2011).

[12] F. Gianotti. *"Physics at the LHC"*. Phys. Rep. 403–404, (2004) 379–399.

[13] G. Jungman et. al. Phys. Rep. 267, (1996).

[14] J. Ellis. *"Particle Physics at Future Colliders"*. arXiv:hep-ex/0210052,2002.

[15] S. Martin. *"A Supersymmetry Primer"*. arXiv:hep-ph/9709356v1,1997.

[16] H. P. Nilles. Phys. Rep. 110, (1984) 1.

[17] H. E. Haber and G.L. Kane. Phys. Rep. 117, (1985) 75.

[18] J. Ellis et. al. Phys. Lett. B121, (1983) 123.

[19] The ATLAS Collaboration. *"Expected Performance of the ATLAS Experiment, Detector, Trigger and Physics"*. CERN–OPEN–2008–020, Geneva, 2008.

[20] C. Potter. *"The Search for Evidence of Supersymmetry in Trilepton Final State at the LHC"*. PhD Thesis, 2009.

[21] The ATLAS Collaboration. *"The ATLAS Experiment at the CERN Large Hadron Collider"*. JINST3 S08003, 2008.

[22] ATLAS collaboration. *"Detector and Physics Performance Technical Design Reports"*. CERN/LHCC/99–014, CERN/LHCC/99–015.

[23] The ATLAS Fact Sheet. http://atlas.ch.

[24] The ATLAS Experiment at CERN. http://atlas.ch.

[25] A. Martin et. al. *"Uncertainties of predictions from parton distributions. II: Theoretical errors"*. Eur. Phys. J C35 (2004) 325–348, .

[26] `http://atlasexperiment.org/index.html`.

[27] S. George. *"The ATLAS High Level Trigger Configuration and Steering Software: Experience with 7 TeV Collisions"*. ATL–DAQ–PROC–2010–053.

[28] The ATLAS Collaboration. *"ATLAS Computing: Technical Design Report"*. ATLAS–TDR–017 CERN-LHCC–2005–022, 2005.

[29] T. Sjostrand, S. Mrenna and P. Skands. *"PYTHIA 6.4 Physics and Manual"*. JHEP 0605 (2006) 026.

[30] T. Sjostrand. *"The PYTHIA Event Generator, CDF/D0 Monte Carlo Tutorial"*. Fermilab, 2004.

[31] S. Agostinelli et. al. *"Geant4 – a simulation toolkit"*. Nucl. Instrum. and Meth. A506 (2003) 250–303, .

[32] E. Richter-Was et. al. *"ATLFAST 2.0 a fast simulation package for ATLAS"*. ATL–PHYS–98–131, 1998.

[33] S. Dean and P. Sherwood. `http://www.hep.ucl.ac.uk/atlas/atlfast/`.

[34] S. Hassani et. al. *"A Muon identification and reconstruction procedure for the ATLAS detector at the LHC using the MUONBOY, STACO and MuTag reconstruction packages"*. Nucl. Instrum. Meth. A572 (2007) 77, .

[35] M. Cacciari and G. Salam. *"The anti-k_t jet clustering algorithm"*. `arXiv:hep-ph/0802.1189v2,2008`.

[36] ATLAS Experiment. *The Etmiss twiki.* `https://twiki.cern.ch/twiki/bin/view/AtlasProtected/EtMiss`.

[37] AMI ATLAS Production. `https://atlas-ami.cern.ch/`.

[38] P. de Jong et. al. *"Data-driven determinations of W, Z, and top background to Supersymmetry searches at the LHC"*. ATL–COM–PHYS–2008–109.

[39] V. Boisvert (ATLAS UK Top Physics). Private Communication.

[40] G. Hahn and S. Shapiro. *Statistical Models in Engineering*. John Wiley and Sons, 1967.

[41] F. James and M. Roos. *"Minuit: A System for Function Minimization and Analysis of the Parameter Errors and Correlations"*. Comput. Phys. Commun. 10, 343–367 (1975).

[42] G. Cowan. *Statistical Data Analysis*. Oxford University Press, 1998.

[43] G. Cowan et. al. *"Asymptotic Formulae for Likelihood-Based Tests of New Physics"*. . `arXiv:1007.1727v2,2010`.

[44] G. Cowan. *"SigCalc, a program for calculating discovery significance using profile likelihood"*. `http://www.pp.rhul.ac.uk/~cowan/stat/SigCalc/`.

[45] The ATLAS Collaboration. *Searches for supersymmetry with the ATLAS detector using final states with two leptons and missing transverse momentum in* $\sqrt{s} = 7$ *TeV proton-proton collisions."*. `arXiv:hep-ex/1110.6189v1,2011`.

[46] A. H. Chamseddine et. al. Phys. Rev. Lett. 49, 970 (1982).

[47] G. L. Kane et. al. Phys. Rev. D 49, 6173 (1994).

[48] A. L. Read. J. Phys.G G28, (2002) 2693-2704.